Wetting Hysteresis and Droplet Roll Off Behavior on Superhydrophobic Surfaces

by

Katherine Marie Smyth

Submitted to the Department of Mechanical Engineering
in partial fulfillment of the requirements for the degree of

Bachelor of Science in Engineering as Recommended by the
Department of Mechanical Engineering

at the

MASSACHUSETTS INSTITUTE OF TECHNOLOGY

June 2010

Author.....
Department of Mechanical Engineering
May 10, 2010

Certified by.....
Kripa K. Varanasi
Assistant Professor
Thesis Supervisor

Accepted by.....
John H. Lienhard V
Collins Professor of Mechanical Engineering;
Chairman, Undergraduate Thesis Committee

Wetting Hysteresis and Droplet Roll Off Behavior on Superhydrophobic Surfaces

by

Katherine Marie Smyth

Submitted to the Department of Mechanical Engineering
on May 10, 2010, in partial fulfillment of the
requirements for the degree of
Bachelor of Science in Engineering as Recommended by the Department of Mechanical Engineering

ABSTRACT

Various states of hydrophobic wetting and hysteresis are observed when water droplets are deposited on micro-post surfaces of different post densities. Hysteresis is commonly defined as the difference between the advancing and receding contact angle and after many decades of research, the mechanisms governing hysteresis are still not fully understood. Particularly, stick-slip behavior of the three-phase contact line has been observed and qualitatively attributed to surface or chemical heterogeneities, but the behavior has yet to be quantified. In this thesis, contact line motion particularly focused on stick-slip behavior and its influence on drop width and contact angle was examined as a new approach to understanding hysteresis as pertaining to micro-textured surfaces. This work focuses on developing a fundamental understanding and physical model of the stick-slip behavior of the contact line and preliminarily explores the influence of contact line velocity on this stick-slip behavior and contact angle. By characterizing stick-slip behavior and hysteresis on micro-post surfaces, models can be developed that in the future can aid in surface design for optimal wetting behavior in industrial and power plant applications. Additionally, the pinning parameter has been used to predict roll off angle on micro-post surfaces for a variety of post densities and these predictions have been experimentally verified. With further definition of the pinning parameter to include surface roughness and impact phenomena, the pinning parameter can be used in surface design for droplet shedding in industrial applications.

Thesis Supervisor: Kripa K. Varanasi
Title: Assistant Professor

ACKNOWLEDGEMENTS

I would first and above all like to thank Professor Varanasi for his enthusiasm and continued support throughout the project. With his busy schedule, he still took the time to sit with me for hours to discuss surface wetting and give me firm direction throughout my thesis project.

I could not have completed this project and realistically, I would have never been a part of it without Adam Paxson. It was his kind words that encouraged Professor Varanasi to take me on as a thesis student and Adam's help on anything and everything related to my thesis has been invaluable. I would also like to thank all of the members of the Varanasi Group for their positive attitude and the collaborative work environment that I have truly appreciated being a part of. For technical support, I want to thank Dr. Jim Bales of the Edgerton center for use of the high speed camera.

Finally, I wish to thank my friends and family for their support throughout my undergraduate years at MIT. My friends have listened to me when stressed with school and accepted my continued flaking on social events for most of the semester to work on this thesis. Although my family might not know or fully understand what I have been working on, they continue to support me and I could not have made it through these four years without them.

CONTENTS

LIST OF FIGURES

LIST OF TABLES

1 Introduction

1.1 History and motivation

Young initially derived the equation for contact angle based on surface free energies, and later studies in surface wetting in the early half of the twentieth century by Cassie, Baxter, and Wenzel contributed to the definition of contact angle as part of work for the textile industry. The measurement of contact angle has applications to the study of dropwise condensation where the energy barrier of nucleation is attributed to the wetting behavior of the solid-liquid contact, and nucleation rate is a function of contact angle [1]. Recently, surface wetting has been examined in microfluidic devices for lab-on-chip applications where thermal gradients and electrowetting have been applied to device surfaces to move water droplets [2]. Surface gradients have also been used to create directions of increasing surface energy enabling water droplets to run uphill [3]. All these applications have a basis in the contact angle equations derived by Young, Cassie, Baxter and Wenzel.

The current work focuses on surface wetting properties with applications to power and water desalination plants. In geothermal, nuclear and water desalination plants, condensation forms films on tank surfaces impeding heat transfer and resulting in energy loss and decreased plant efficiency. Micro- and nano-textured surfaces have been developed to optimize and control surface wetting properties. With the determination of optimal wetting properties and appropriate manufacturing, micro- and nano-textured surfaces could be applied to tank surfaces to prevent film formation significantly increasing plant efficiencies.

1.2 Contact angle equations

For a liquid drop deposited on a solid surface, the contact angle is measured along the boundary of the solid-liquid-vapor (three-phase) contact line. The Young equation for contact angle is derived from the balance of surface tensions acting on the three-phase contact line or the balance of surface free energies with displacement dx of the contact line (see equation 1.1 below). Schematics of contact angle measurement are shown in Figure 1-1 and Figure 1-2 [4].

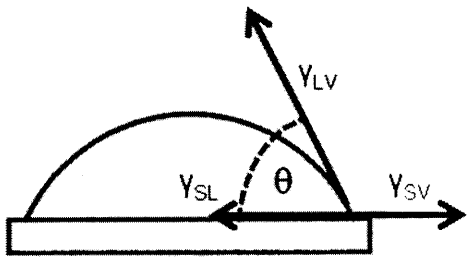

Figure 1-1: Sessile drop on solid substrate with contact angle θ, liquid-vapor surface tension γ_{LV}, solid-liquid surface tension γ_{SL}, and solid-vapor surface tension γ_{SV}.

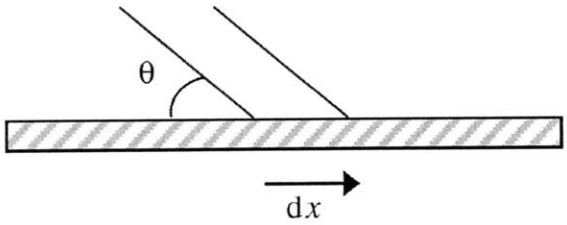

Figure 1-2: Movement of liquid contact line dx along a solid surface.

$$dE = (\gamma_{SL} - \gamma_{SV}) \cdot dx + \gamma_{LV} \cdot dx \cdot \cos\theta \tag{1-1}$$

$$\cos\theta = \frac{\gamma_{SV} - \gamma_{SL}}{\gamma_{LV}} \tag{1-2}$$

The Young equation is modeled for an ideal case assuming that the solid surface is smooth and free of heterogeneities.

Wenzel extended the definition of contact angle to include the influence of surface roughness by introducing the roughness factor, R:

$$R = \frac{\text{actual surface}}{\text{geometric surface}} \tag{1-3}$$

where the actual surface is the area of the solid substrate in contact with the liquid and the geometric surface is the total area of the interface. The roughness factor is included in the Wenzel equation for contact angle:

$$\cos\theta^* = R \cdot \cos\theta \tag{1-4}$$

where θ^* is the observed contact angle [5].

Cassie and Baxter considered the influence of porosity and heterogeneities on the observed contact angle. In considering porosity, σ_1 is the area of the solid-liquid contact with contact angle θ_1 and σ_2 is the area of the liquid-vapor interface attributed to porosity [6].

$$\cos\theta = \sigma_1 \cdot \cos\theta_1 - \sigma_2 \tag{1-5}$$

The contact angle definition for porous surfaces can be expanded to include surface heterogeneities. For a heterogeneous surface, σ_2 becomes the area of the solid-liquid interface with contact angle θ_2, and additional areas and contact angles are added to the equation depending on the number of heterogeneities [7].

$$\cos\theta = \sigma_1 \cdot \cos\theta_1 + \sigma_2 \cdot \cos\theta_2 + \ldots \tag{1-6}$$

More recently, models have been developed to describe the molecular interactions between the liquid and solid substrate that determine contact angle. Polarities of a liquid

and solid surface are defined by the Lewis acid and base parameters for free surface energy.

γ^+ = Lewis acid parameter of surface free energy
γ^- = Lewis base parameter of surface free energy
γ^{LW} = total surface free energy

For a liquid, contact angle is defined by:

$$\gamma_l \cdot (1+\cos\theta) = 2 \cdot \left(\sqrt{\gamma_s^{LW} \cdot \gamma_l^{LW}} + \sqrt{\gamma_s^+ \cdot \gamma_l^-} + \sqrt{\gamma_s^- \cdot \gamma_l^+} \right) \tag{1-7}$$

where γ_l is the total surface tension of the liquid and γ_s^+, γ_l^+, γ_s^-, and γ_l^- denote the acid and base parameters for the liquid and solid. The determination of γ^{LW} is slightly more complicated but also depends on the polarity of the liquid and solid. For an apolar liquid on an apolar solid:

$$\gamma_s^{LW} = \gamma_l^{LW} \cdot \frac{(1+\cos\theta)^2}{4} \tag{1-8}$$

and for a polar liquid on an apolar solid:

$$\gamma_l^{LW} = \frac{\gamma_l^{\,2} \cdot (1+\cos\theta)^2}{4 \cdot \gamma_s^{LW}} \tag{1-9}$$

Good discusses the application of these equations to the contact angle measurement of water, glycerol and diiodomethane on corona-treated and untreated polyolefin films [8].

Based on the contact angle measurement, surface wetting characteristics of the liquid-surface interaction can be separated into categories. For a contact angle less than 90°, the liquid-solid interaction is hydrophilic, and for a contact angle greater than 90°, the interaction is hydrophobic. In special cases where the contact angle is between 150° and 180° and contact angle hysteresis is low, the interaction is described as superhydrophobic [9].

1.3 Hysteresis definition and dependence

The definitions for contact angle from the previous section discount the effects of hysteresis. When a droplet is deposited on a surface, it exhibits a contact angle between an advancing and receding value. The difference between the advancing (θ_a) and receding (θ_r) values is the contact angle hysteresis, $\Delta\theta$:

$$\Delta\theta = \theta_a - \theta_r \tag{1-10}$$

Hysteresis is commonly attributed to surface roughness or chemical heterogeneities on the surface of the substrate, but there is some disagreement as to the exact relationship. It is agreed that hysteresis results from pinning at the three-phase contact line, and the dynamic observation of hysteresis shows a "stick-slip" behavior where the three-phase contact line "sticks" until dynamic wetting causes the line to periodically "slip" until it "sticks" again and the cycle repeats. Stick-slip behavior is generally observed when adding or removing volume from a liquid drop, with drop movement on a gradient surface or tilting stage, or with droplet evaporation [10].

The existence of energy barriers caused by roughness and surface irregularities resulting from heterogeneities can explain the stick-slip behavior of contact line motion. Energy barriers on the substrate surface trap the three-phase contact line at a location with a particular free energy until the droplet free energy changes causing the contact line to slip to an alternate surface location associated with a new free energy. The difference in energy between surface locations is the energy barrier that prevents droplet motion resulting in "stick-slip" behavior in dynamic wetting.

Dettre and Johnson constructed heterogeneous surfaces by alternating bands of varying surface tension. Energy barrier heights were calculated from equations derived by integrating the equilibrium force values between surfaces. The resulting curves for advancing and receding contact angle were plotted based on energy barrier [11].

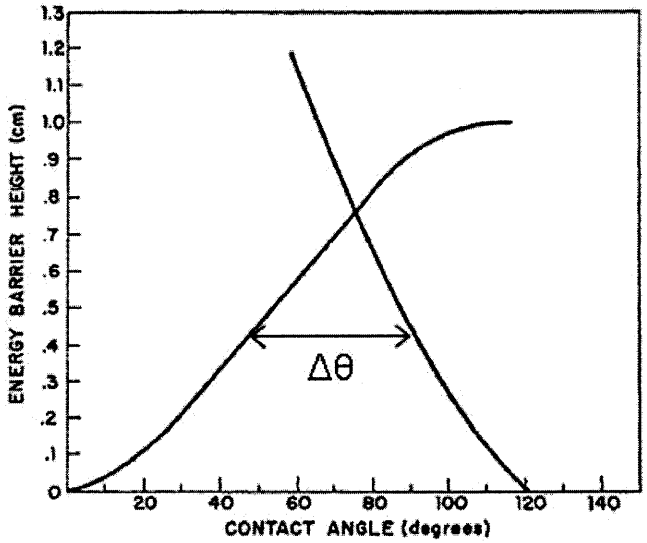

Figure 1-3: Advancing and receding contact angles vs. energy barrier height as calculated by Dettre and Johnson.

At each barrier height, the difference between the advancing and receding angle changes implying that hysteresis is dependent on energy barrier height. Dettre and Johnson further describe hysteresis as dependent on the relative proportions and surface distribution of high and low contact angle regions, surface energies, surface tension of wetting liquid, and vibration energy associated with movement of the three-phase contact line. Hysteresis also depends on the absolute value of the energy barriers which is proportional to the size of the contact angle regions and surface tension of liquid [55].

Separate from energy barrier theory, perturbations of the contact line based on asperity size and shape have been used to describe hysteresis and contact line motion. Joanny and de Gennes developed the spring constant of the contact line based on the Laplace condition at the liquid-solid interface and a capillary energy correction factor. Based on the spring constant, the effect of weak and strong heterogeneities on hysteresis was analyzed by introducing random fluctuations of the work of adhesion into the system. For weak surface heterogeneities, small perturbations were present in the contact line but had a negligible influence on hysteresis and overall contact line motion. For strong heterogeneities, defect distribution and shape created large perturbations that affected contact angle hysteresis and contact line motion. The model was derived considering surface contamination as the cause of heterogeneities [13]. Collet et al employ a numerical simulation of a disordered system to examine random trapping of the three-phase contact line. The contact line remains trapped for a random time with exponential distribution until the contact line rapidly snaps to another trap [14].

Partially encompassing energy barrier and contact line perturbation theories, the definition of hysteresis can be divided into mechanical and chemical definitions. Chemical hysteresis occurs when molecules at the liquid-solid interface rearrange or relax to a new equilibrium different from the equilibrium before wetting. Mechanical hysteresis is caused by retentive forces on the contact line that can be attributed to surface impurities, asperities and roughness [15]. Chemical hysteresis varies from mechanical hysteresis because the chemical groups at the surface change between the pre- and post-wetting states, and chemical hysteresis can occur on smooth and chemically homogeneous surfaces [16]. On chemically homogeneous surfaces, Chen et al found that low hysteresis was exhibited on solids where surface groups were completely immobile or easily free to reorient [15].

Alternative equations have also been derived to describe hysteresis. Extrand provides additional empirical and thermodynamic equations. Hysteresis can be determined by the difference of cosines:

$$\Delta \cos\theta = \cos\theta_r - \cos\theta_a \tag{1-11}$$

or in a dimensionless form often referred to as reduced hysteresis, H:

$$H = \frac{\theta_a - \theta_r}{\theta_a} \tag{1-12}$$

Using the Young equation, the work of adhesion due to hysteresis provides a thermodynamic based definition:

$$\Delta W = \gamma_l \cdot \left(\cos\theta_r - \cos\theta_a\right) \tag{1-13}$$

The common definition of contact angle hysteresis is most widely used, but some recent work has looked at reduced hysteresis to examine polymeric surfaces [10]. Extrand and Kumagai examined hysteresis on various polymeric surfaces with contact liquids of varying viscosity, molecular volume, volatility, and polarity to find that the reduced

hysteresis parameter was similar on all surfaces suggesting that the reduced hysteresis is independent of contact liquid. This independence suggests that hysteresis is an intrinsic property of liquid-solid interaction and that roughness is an unlikely cause of hysteresis [17].

1.4 Hysteresis and the pinning parameter

Tribological properties including the adhesion and friction properties of surfaces are suggested to affect hysteresis and wetting behavior. Wetting creates menisci at the solid-liquid interfaces that increase the adhesion and friction between two sliding solids [9]. Wetting and dewetting processes can also be described using Newton's first and second laws. When a water droplet slides on a tilted plane, potential energy is converted to heat, friction and kinetic energy satisfying the second law. Contact line behavior and therefore droplet movement is dictated by maintaining free energy equilibrium between the drop and surface satisfying the first law. Inherent limits on wetting and dewetting also exist to maintain mechanical equilibrium again satisfying the first law [18].

Varanasi et al introduced the pinning parameter to describe wetting behavior at a solid-liquid interface similar to the use of the coefficient of friction to describe solid-solid interactions. The pinning parameter is derived from the balance of forces acting on a drop immediately before sliding or rolling behavior on an inclined surface.

$$\rho \cdot g \cdot V \cdot \sin\alpha = \pi \cdot \gamma_l \cdot r \cdot (\cos\theta_r - \cos\theta_a) \tag{1-14}$$

ρ, g, V, α, and r are the drop density, gravitational constant, volume, tilt angle, and radius of the contact patch respectively. From the above equation, μ is described as:

$$\mu = \frac{\gamma_l}{2} \cdot (\cos\theta_{rs} - \cos\theta_{as}) \tag{1-15}$$

where θ_{rs} and θ_{as} are the receding and advancing angle measured on a smooth surface. With this definition, Varanasi et al. have experimentally obtained μ for a few water-solid interactions.

Surface	μ (mN/m)	
	mean	Std dev
Silicon	6.3	0.4
Silicon/FS	20.1	1.8
PDMS	22.5	0.4
Lexan	12.8	1.7

Table 1-1: μ calculated for various water-solid interactions by Varanasi et al [19].

1.5 Contact angle measurement techniques

The sessile drop approach is used to measure contact angle by depositing a small droplet of liquid onto a solid substrate. Volume addition and subtraction and the tilting base techniques measure advancing and receding contact angle of sessile drops.

In the volume addition and subtraction technique, volume is added and the droplet expands asymptotically approaching the value of the advancing contact angle. When volume is withdrawn, the contact angle recedes approaching a minimum value referred to as the receding contact angle. Volume deposition is generally performed with a microsyringe or micropipette.

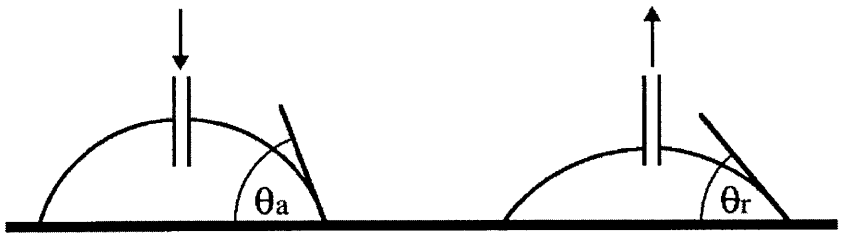

Figure 1-4: Left: volume is added to measure advancing contact angle. Right: volume is subtracted to measure receding contact angle [20].

With the tilting base technique, a drop of constant volume is deposited onto a solid substrate fixed to a tilting base initially oriented horizontally. The base is tilted until the drop begins to roll or slide along the surface. At the moment immediately preceding the incipient motion of the drop, the advancing and receding angle are recorded by measuring the contact angle on either side of the droplet as shown below:

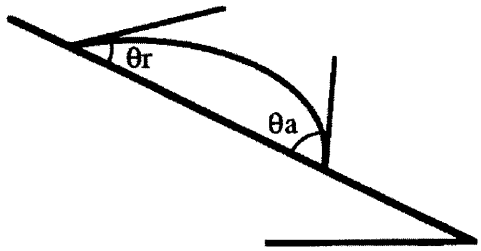

Figure 1-5: Advancing and receding contact angle measurement on tilt stage immediately before incipient droplet motion [17].

Some discrepancies have been observed in the measurement of advancing and receding contact angle between techniques. Measurements of advancing angle with the tilting base technique have exceeded advancing angles with volume addition. Similarly, a theoretical approach based on surface heterogeneities and two-dimensional droplet geometry predicted that advancing contact angle with the tilting base method can be lower than the advancing angle with volume addition, and receding angle with the tilting base method can be higher than the receding angle with volume subtraction. ElSherbini and Jacobi separately define θ_{min} and θ_{max} as the critical angles before the initial drop motion on a tilting base separately from θ_r and θ_a [21].

Other techniques exist to measure contact angle including the rotating plate method used by Wenzel [5] and the Wilhelmy plate method where a vertical plate is

slowly withdrawn from a liquid and the contact angle of the liquid meniscus on the disc is measured. Alternatively, a liquid bridge at the tip of an AFM can be used to measure contact angle and liquid surface tension.

1.6 Uncertainties in contact angle measurement

The factors contributing to hysteresis described for hysteresis in Section 1.3 are known to exist, but in many cases, an explicit relationship is not fully defined. Particularly, the relationship between contact angle and contact line velocity is not well known. Hydrodynamic and molecular-kinetic theories provide two definitions of contact line velocity. In Cox's viscous theory based on hydrodynamics, contact line motion is assumed to be steady and advancing on a smooth surface. Cox's equation relates the hydrodynamic length scale (L_H), slip length (L_s), and capillary (Ca) and Reynolds (Re) numbers to a function of contact angle. The angle function, $g_v(\theta)$, is defined as:

$$g_v(\theta) = \int_0^{\theta} \frac{\phi - \sin\phi \cdot \cos\phi}{2 \cdot \sin\phi} \cdot d\phi \tag{1-16}$$

and Cox's simplified equation is:

$$Ca \cdot \ln\left(\frac{L_H}{L_S \cdot \mathrm{Re}}\right) = g_v(\theta^*) - g_v(\theta) \tag{1-17}$$

where θ^* is the contact angle in the transitional region where inertia and viscous effects are on the same order.

Molecular-kinetic theory assumes that contact line movement results from molecules on the solid quickly transitioning from the liquid to the vapor side of the contact line. Again, the assumption is made that the contact line is advancing. The velocity of the contact line (V_{CL}) is explicitly stated as:

$$V_{CL} = 2 \cdot \kappa_w \cdot \lambda \cdot \sinh\left[\frac{\gamma_l}{2 \cdot n \cdot k \cdot T} \cdot (\cos\theta_E - \cos\theta)\right] \tag{1-18}$$

where κ_w, λ, n, k, T, θ_E and θ are the frequency, individual molecular displacement length, number of absorption sites per unit area, Boltzmann's constant, absolute temperature, equilibrium contact angle and contact angle between the equilibrium and advancing contact angle respectively [22].

Each theory that relates contact angle to contact line velocity fails to describe contact line behavior outside of particular regimes. In Cox's equation, contact line velocity can only be determined when the inertial and viscous forces are on the same order, and the contact angle is advancing on a smooth surface. In molecular-kinetic theory, the velocity is derived only for contact angles between the equilibrium and advancing values. Both models directly or indirectly assume that contact line motion is steady, which contrasts with the "stick-slip" behavior observed with hysteresis, and

neither model considers the relation of contact line velocity to advancing and receding contact angles.

More recently, a lattice Boltzmann model (LBM) developed by Zhang and Kwok numerically computed the behavior of contact line velocity on superhydrophobic, micro-post channel surfaces. Zhang and Kwok considered both the hysteresis and the stick-slip behavior of the contact line motion in the LBM model resulting in the definition of two regimes. For void space ratio $r_v<0.5$, contact line velocity decreased with increasing void space ratio and with $r_v>0.5$, the contact line velocity decreased with increasing void ratio. The void space ratio r_v is:

$$r_v = \frac{b}{b+a} \tag{1-19}$$

where a is the micro-post width and b is the post spacing [23].

Similar to the uncertainties in contact line velocity measurement, the instability of the receding angle leads to uncertainty in hysteresis and receding contact angle measurement. Drop volume dependence on contact angle is not fully explained especially for the receding angle where volume appears to affect angle measurement more significantly [8]. With evaporation, it is theorized that angles below the receding value can be observed based on the fulfillment of the Gibbs free energy equation [10].

1.7 Wetting on micro- and nano-textured surfaces

Some past work with micro- and nano-textured surfaces is influenced by surface wetting phenomenon on different plant leaves especially leaves exhibiting the "lotus effect," which refers to the superhydrophobic, self-cleaning nature of the leaf surface. The lotus and many other plant species are successfully water repellent because of micro-patterned surfaces and roughness. On these surfaces, contaminating particles adhere to water droplets rolling down the leaf resulting in self-cleaning properties [24]. It is suggested that increasing the roughness of a micro-textured surface results in increased hydrophobicity. The superhydrophobicity of some leaf surfaces has been attributed to the nano-textures present on the micro-patterned surfaces. Hydrophobic and superhydrophobic surfaces of PS and PMMA have been fabricated by mimicking the surface structure of plant leaves [25].

Micro-posts etched onto silicon substrates with hydrophobic coatings can also exhibit superhydrophobic wetting behavior. This superhydrophobicity is created by air pocket formation between posts that results in a lower drop contact area, reduced drag [2], and Laplace pressure in the gaps prevents liquid penetration [23]. Air pocket formation separates the Cassie and Wenzel wetting behaviors on micro-post substrates. When air pockets are present, contact angles are best predicted by the Cassie equation and are thus referred to as in the "Cassie" wetting state. With no air pockets present, the Wenzel equation provides the best prediction for contact angle and the droplet is in the "Wenzel" wetting state. Due to air pocket formation, Cassie droplets exhibit more hydrophobic wetting behavior than droplets in the Wenzel state [25].

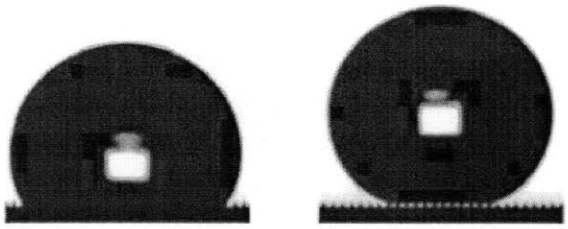

Figure 1-6: Droplets in Wenzel (left) and Cassie (right) wetting states [2].

Extrand defines the transition between the Cassie and Wenzel states by developing criteria for suspension (Cassie) and collapse (Wenzel). For a drop to remain suspended, the surface force directed upward must exceed the body force acting on the droplet. Based on surface and body forces, Extrand developed an equation for critical contact line density (Λ_c) that can be used to determine droplet suspension or collapse. The equation is shown below:

$$\Lambda_c = -\rho \cdot g \cdot V^{\frac{1}{3}} \cdot \frac{\left[\frac{1-\cos\theta_a}{\sin\theta_a} \cdot \left[3+\left(\frac{1-\cos\theta_a}{\sin\theta_a}\right)^2\right]^{\frac{2}{3}}\right]}{(36\cdot\pi)^{\frac{1}{3}} \cdot \gamma_l \cdot \cos(\theta_{a,0}+\omega-90°)} \tag{1-20}$$

where ω is the rise angle on the side of surface asperities and $\theta_{a,0}$ is the true advancing contact angle as calculated in the Wenzel equation. For contact line densities greater than the critical density, droplets remain suspended and for densities below the critical density, droplets collapse into the spacing between posts [26].

Incipient movement of a droplet on a micro-post surface is proposed to be governed by driving force, hysteresis force and viscous drag. Before incipient motion, the droplet remains stationary by the balance of driving and hysteresis forces acting on the front and back edge of the droplet. Upon incipient motion, the change in free energy for a slice of the drop is attributed to film force, hysteresis at the front and back edges and pinning [2].

Separately, Varanasi et al suggest that the pinning parameter can determine the tilt angle for incipient motion with the equation below:

$$\rho \cdot g \cdot V \cdot \sin\alpha = \mu \cdot \beta \cdot 2 \cdot \pi \cdot r \tag{1-21}$$

where β is the texture parameter:

$$\beta = \frac{1}{1+\frac{b}{a}} \tag{1-22}$$

The theoretical Cassie and Wenzel contact angles on micro-post substrates are dependent on post width, height and spacing. For the Wenzel state, contact angle can be calculated with equation 1.4 where the roughness factor, R becomes:

$$R = 1 + \frac{4 \cdot \left(\frac{h}{a}\right)}{\left(1 + \frac{b}{a}\right)^2} \tag{1-23}$$

and h is the micro-post height. The Cassie equation is defined as in equation 1.5 with:

$$\sigma_1 = f_{SL} = \frac{1}{\left(1 + \frac{b}{a}\right)^2} \tag{1-24}$$

$$\sigma_2 = f_{LA} = 1 - \frac{1}{\left(1 + \frac{b}{a}\right)^2} \tag{1-25}$$

In the design of superhydrophobic surfaces, impact is an important consideration for aircraft and automotive applications. For such applications, superhydrophobic surfaces must maintain their wetting properties during drop impact. For superhydrophobicity to be maintained, the capillary pressure must exceed the water hammer pressure (P_{WH}) of the initial impact:

$$P_{WH} = 0.3 \cdot \rho \cdot C \cdot v \tag{1-26}$$

where C is the speed of sound in liquid and v is the liquid velocity. After the initial impact, the pressure from the drop impact is reduced to the Bernoulli pressure (P_B):

$$P_B = \frac{\rho \cdot v^2}{2} \tag{1-27}$$

Depending on the magnitude of each pressure, three different behaviors result based on impact:

$$\begin{aligned} &P_C < P_B < P_{WB} : \text{pinning and complete infiltration} \\ &P_B < P_C < P_{WB} : \text{partial pinning} \\ &P_C < P_{WH} < P_C : \text{complete recoil} \end{aligned} \tag{1-28}$$

where P_C is the capillary pressure [19].

1.8 Objectives

This thesis aims to further understand hysteresis on hydrophobic and superhydrophobic surfaces and to explore the relationship between contact line motion and the advancing and receding contact angle. Hysteresis will be examined as an intrinsic property of a solid-liquid interface and as such, the roll off behavior on various micro-textured surfaces should be predicted by the pinning parameter.

Sessile drop contact angle measurements with the volume addition and subtraction and tilting base techniques will be used to measure advancing and receding contact angle, determine the velocity of the contact line, and to experimentally support the physical phenomena associated with advancing and receding behavior of the contact line. Experimentally determined droplet width and contact angle as a function of time will be examined to explain the motion of the contact line in the advancing and receding cases on smooth and micro-textured surfaces for droplets in the Cassie and Wenzel states. Stick-slip behavior of the contact line during receding in the Cassie state will be further explored by experimentally determining the period and amplitude of this behavior as a function of micro-post density. High speed video of the contact line will show contact line motion in the advancing and receding cases to visually aid in understanding the presence and mechanism behind the stick-slip behavior of the contact line. A preliminary model of stick-slip behavior as a result of the rupture of capillary bridges formed between the drop and micro-post surface will be purposed to physically explain the pinning phenomenon present as a result of hysteresis.

Preliminary experiment with different volume addition and subtraction rates will be completed to explore the relationship between contact line velocity and contact angle. The dependence of the stick-slip phenomena on the velocity of the contact line will be explored with the capillary bridge model derived for stick-slip behavior.

It is the goal of this thesis to fundamentally describe contact line motion and hysteresis on superhydrophobic surfaces for further application to the design of these surfaces. With the ability to understand the mechanisms of advancing and receding behavior, it is hoped that surfaces that exhibit low hysteresis and optimal droplet shedding behavior can eventually be developed for applications in power and water desalination plants where droplet shedding is important to plant efficiency. With this fundamental exploration of hysteresis and contact line motion on superhydrophobic surfaces, it is hoped that wetting phenomena can be further understood physically, experimentally, and theoretically for further industrial applications.

2 Experimental Procedure

2.1 Sample Preparation

Micro-post samples were prepared using standard lithography processing techniques. Positive photoresist was spin coated onto a silicon wafer and a photomask of the post geometry was created with printed chrome on borosilicate glass. The silicon substrate with photoresist and photomask was exposed to UV light, and posts were etched into the developed substrate with deep reactive ion etching. Photoresist was stripped from the surface with piranha cleaning to complete the wafer processing.

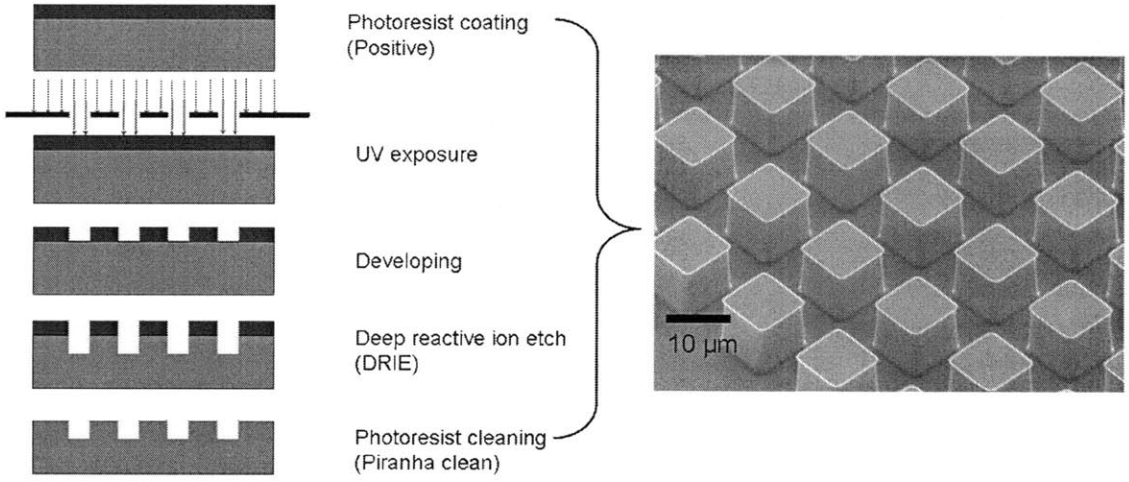

Figure 2-1: Left: outline of lithography processing of micro-post samples (courtesy of Hyuk-Min Kwon). Right: SEM image of micro-post array.

After patterning, a monolayer of trichloro(1H,1H,2H,2H-perfluorooctyl)silane (fluorosilane) was deposited on the micro-post array with a vacuum dessicator making the substrate hydrophobic.

2.2 Goniometer Contact Angle Measurement

Measurements for the volume addition and roll off methods were taken on a ramé-hart Model 500 Advanced Goniometer with DROPimage Advance v2.4 software. A ramé-hart automated dispensing system was used to deposit and add and withdraw volume from droplets, and a ramé-hart automated tilting base was used for roll off measurements.

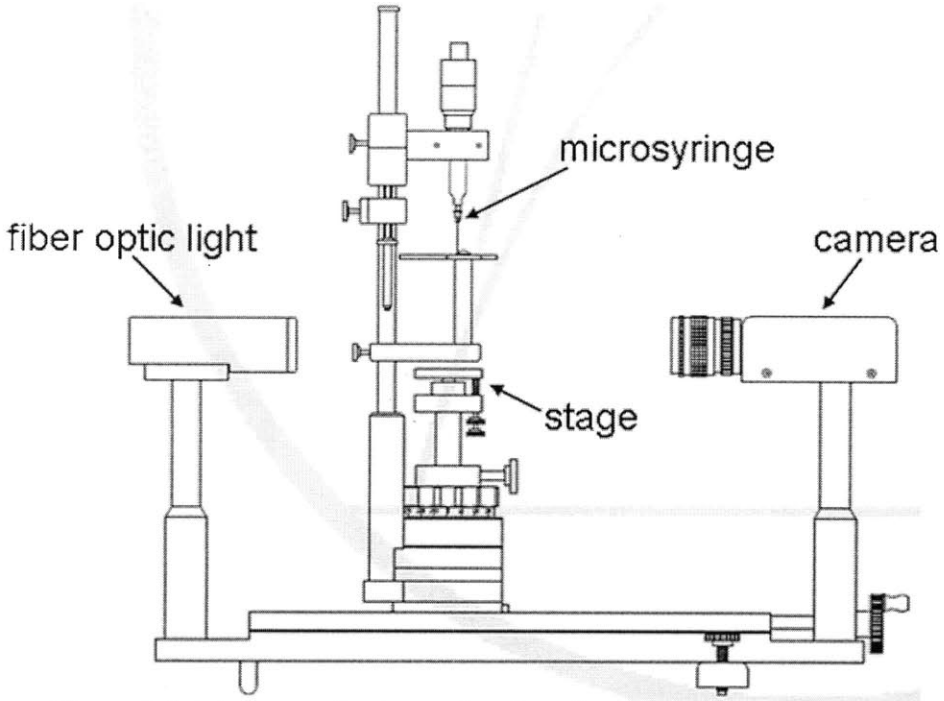

Figure 2-2: Picture and schematic of goniometer measurement system [27].

The goniometer was placed on a Newport CM-225 Ultra-clean vibration damping system with four isolators to reduce the effects of ambient vibration on contact angle measurement, and a transparent Lexan shade was fabricated and placed over the stage to reduce the effects of air flow.

For volume addition experiments, the automated dispensing system and the DROPimage software were operated on two separate computers, which allowed measurements to be taken discretely during continuous volume addition and subtraction. The rate of volume addition and subtraction was controlled by changing the stroke time in the automated dispensing system interface.

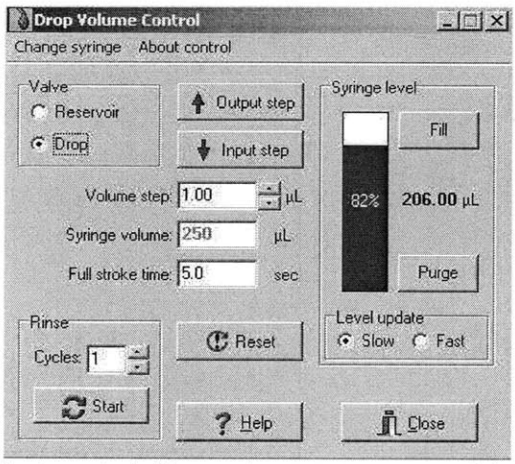

Figure 2-3: Automated dispensing system control interface [27].

For all experiments, a 250μL syringe was used in the dispensing system. The full stroke time refers to the amount of time required to fully dispense the syringe volume. The volume addition and subtraction rate can be simply calculated by dividing the volume (250μL) by the full stroke time, and therefore, increasing stroke time will result in a slower volume addition rate. It is assumed that the contact line velocity is dependent on volume addition rate, so increases in volume addition rate and therefore decreases in stroke time increased contact line velocity.

Experiments were performed on micro-structured and smooth silicon substrates coated with a monolayer of fluorosilane. The micro-structured surfaces were patterned with 10 μm by 10 μm by 10 μm rectangular micro-posts with 3.3, 5, 7.5, 10, 15, 20, 25, 30, 40, 50, 75, and 100 μm spacing between posts. Advancing and receding contact angles were measured on each substrate using the volume addition and subtraction method measurement technique specified in Appendix Section 7.4, and the roll off angle measurement technique specified in Appendix Section 7.5.

For the volume addition and subtraction method, the influence of contact line velocity on contact angle measurement was investigated by varying the volume addition and subtraction rate. Stroke times of 1200, 900, 600, 100, and 20s were used to achieve volume addition and subtraction rates of 0.208, 0.292, 0.417, 2.5, and 12.5 μL/s respectively on each substrate. For the 1200s and 600s stroke time experiments, a 30 gauge stainless steel needle was used, and a 31 gauge superhydrophobic needle was used for all other trials. In the roll off method, the effect of tilt angle rate on contact angle measurements was investigated by varying the angle increment used for each trial. The angle increment refers to the difference between the initial and final angle specified at the start of the experiment. Angle increments of 5 and 10 degrees were examined, which correspond to title angle rates of 0.1°/s and 0.2°/s respectively.

Further details about zeroing, sample and drop placement, and the overall measurement process are provided in the Appendix Section 7.

2.3 High Speed Video

Video of the contact line during volume addition and subtraction was taken with a Phantom High Speed Video camera fitted with a Navitar lens including a 6.5X zoom, 3mm Fine Focus axial distance body tube, 2.0X lens attachment, and 2.0X F-mount adapter. Lighting was provided by a fiber-optic light source with diffusing glass. The light and high speed camera were oriented about the goniometer stage as shown below:

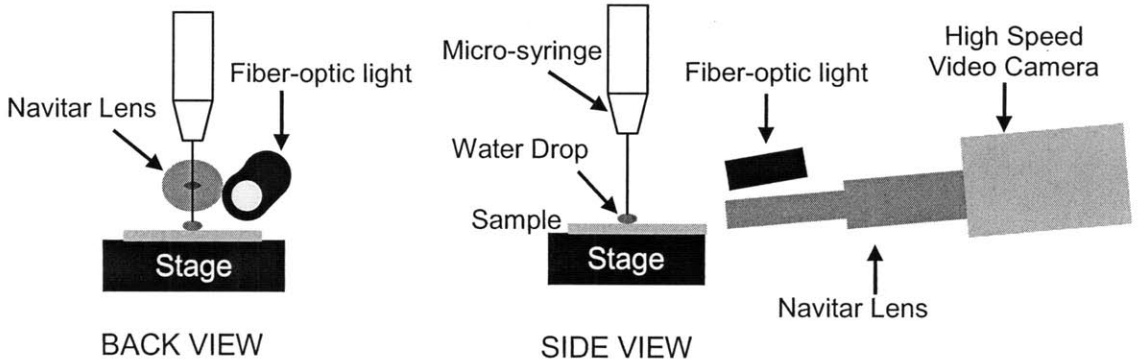

Figure 2-4: Lay out of high speed video set-up.

A water drop was deposited on the goniometer stage using the automated drop dispensing system. Trials were completed at 600 and 1200s full stroke times on the 10 μm by 10 μm by 10 μm rectangular micro-posts with 10 and 50 μm.

Videos were taken at a frame rate of 200 frames per second, at the maximum exposure time of 1247 μs, resolution of 800x600, and zoom was chosen to fit the screen. Other parameters such as EDR exposure, contrast, and brightness were modified to reduce the appearance of bright spots in the frame. Bright spots were common and caused by the reflection of light off the water droplet.

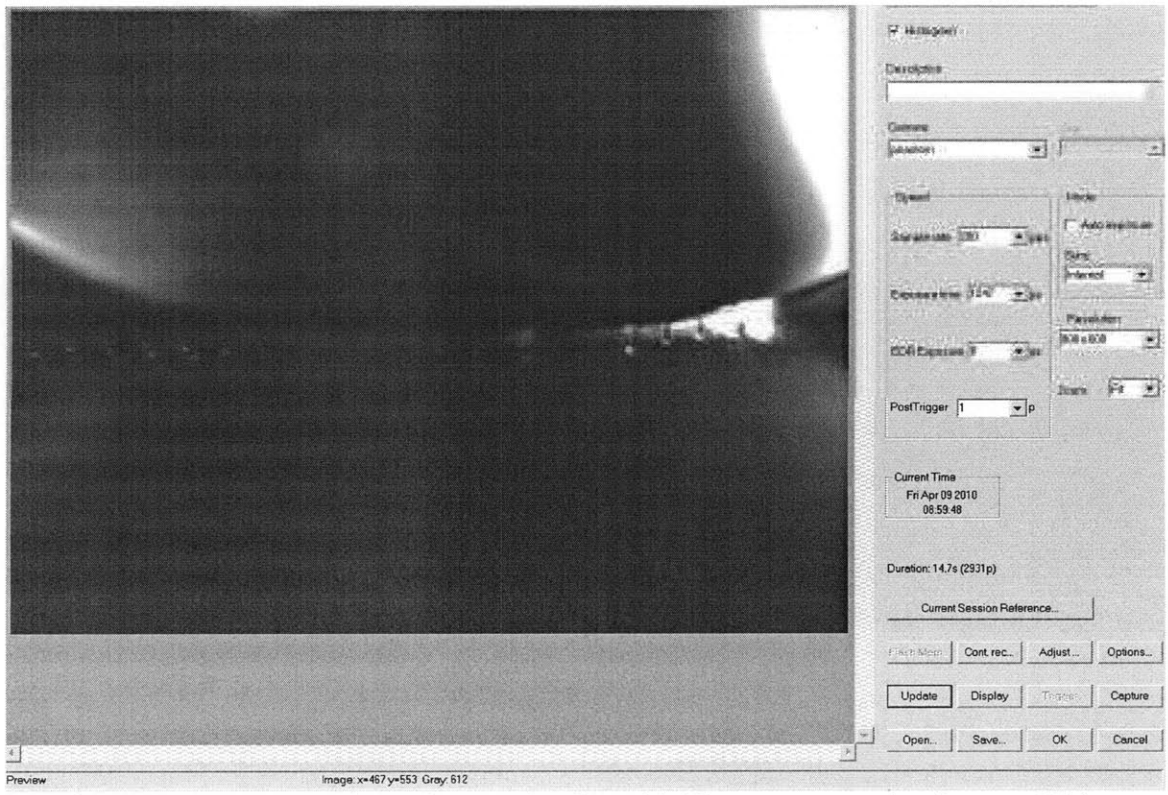

Figure 2-5: Image preview of water droplet with Phantom control software. Video parameters are shown on the right.

3 Roll Off Behavior on Superhydrophobic Surfaces

3.1 Detailed Derivation of the Pinning Parameter

Roll off behavior is important for dynamic applications in power plants and other industries where condensation heat transfer leads to reduced efficiency. If droplets could be easily shed from surfaces in these applications, heat transfer could be greatly improved resulting in higher plant efficiencies. Prediction of the roll off angle in a static case is a start to understanding the shedding behavior and improving the design of surfaces for these industrial applications.

With the pinning parameter μ described in Section 1.4, roll off angle can be predicted on a textured surface based on parameters determined for a smooth surface. The pinning parameter μ can be further described as the pinning force per unit length, and is derived similarly to Young's equation for contact angle on a smooth surface.

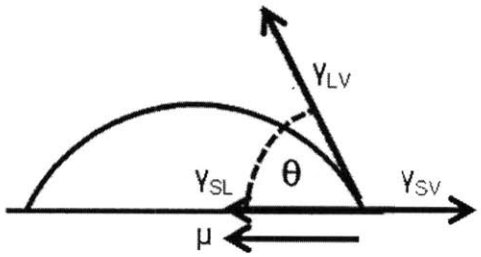

Figure 3-1: sketch of surface tensions and pinning parameter acting on contact line.

From the parameters acting at the contact line, a balance of forces per unit length is determined for the advancing and receding cases on a smooth surface:

$$\gamma_{SV} = \gamma_{LV} \cdot \cos\theta_{as} + \gamma_{SL} + \mu \tag{3-1}$$

$$\gamma_{SV} = \gamma_{LV} \cdot \cos\theta_{rs} + \gamma_{SL} - \mu \tag{3-2}$$

The sign of the pinning parameter changes to resist the motion of the contact line in the advancing and receding cases. Equations 3-1 and 3-2 are set equal to determine the pinning parameter resulting in equation 1-15.

The pinning force resists the incipient motion of the drop and is determined from μ and the effective pinning length along the contact line, l_e.

$$\rho \cdot g \cdot V \cdot \sin\alpha = \mu \cdot l_e \tag{3-3}$$

It should be noted that the equation above is valid for the equilibrium state immediately before the drop begins to roll off the surface.

For applications to superhydrophobic, textured surfaces, the effective length is determined geometrically from the micro-post width and spacing.

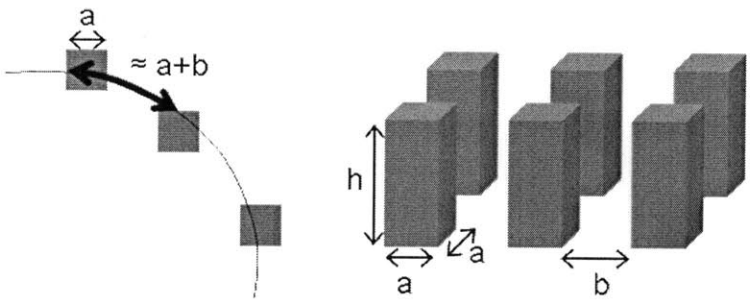

Figure 3-2: Left: contact line resting on micro-post structures. Right: geometry of micro-posts.

For the Cassie state, the effective length is computed from the radius of the total contact patch and the fraction of the patch in contact with the drop referred to as the texture parameter β defined in equation 1-22. The texture parameter is derived from the sketch on the left in Figure 3-2 where the fraction of the patch in contact with the drop is roughly the width of the post divided by the width and post spacing. With the texture parameter, the effective pinning length can be written as:

$$l_e = \beta \cdot 2 \cdot \pi \cdot r \tag{3-4}$$

This definition of effective length can be substituted into equation 3-3 resulting in the equation for roll off angle given by equation 1-21.

3.2 Experimental Determination of μ and Roll Off Angle

Varanasi et al determined the pinning parameter for various liquid-solid interfaces as shown in Table 1-1 [19]. The pinning parameter was calculated experimentally and compared to the values determined by Varanasi et al with a variety of volume addition and subtraction rates for water on bare silicon and silicon coated with a fluorosilane monolayer.

	μ (N/m)	
	Bare Silicon	Silicon with Fluorosilane
Varanasi et al	0.0063	0.0201
0.208 μL/s	0.0097	0.0237
0.292 μL/s	-	0.0219
0.417 μL/s	0.0082	0.0234
2.5 μL/s	0.0073	0.0221
12.5 μL/s	-	0.0207

Table 3-1: Experimentally calculated values of μ.

Errors in the calculation of μ likely result from goniometer measurements, which have an error of ±2° [9]. Values of the pinning parameter of water on silicon with fluorosilane fall within two standard deviations of the pinning parameter determined by Varanasi et al [19].

Contact angle roll off experiments on textured surfaces were completed with the goniometer and compared with predicted roll off angles determined by the pinning parameter and the theoretical Cassie contact angle. The theoretical Cassie contact angle in complete form is written as:

$$\cos\theta_C = f_{SL} \cdot \cos\theta_0 - f_{LA} \tag{3-5}$$

where θ_C is the Cassie contact angle, θ_0 is the equilibrium contact angle on a smooth surface, and f_{SL} and f_{LA} are defined by equations 1-24 and 1-25 respectively [19]. The roll off angle is more explicitly computed with the equation:

$$\sin\alpha = \frac{2 \cdot \pi \cdot \mu \cdot \beta}{\rho \cdot g} \cdot \left(\frac{3}{\pi \cdot V^2}\right)^{\frac{1}{3}} \cdot f(\theta) \tag{3-6}$$

with the function f(θ) given as:

$$f(\theta) = \frac{\sin\theta}{\left(2 - 3 \cdot \cos\theta + \cos^3\theta\right)^{\frac{1}{3}}} \tag{3-7}$$

The contact patch radius is eliminated from equation 1-21 and simplified resulting in equation 3-6 [19]. Contact patch radius is eliminated by substituting r for the following equation derived from the volume of a spherical cap:

$$r = \sin\theta \cdot \left[\frac{3 \cdot V}{\pi \cdot \left(2 - 3 \cdot \cos\theta + \cos^3\theta\right)}\right]^{\frac{1}{3}} \tag{3-8}$$

The detailed derivation of r is provided in Appendix Section 8.

Fluorosilane coated silicon micro-post surfaces were used in experiment and the pinning parameter for water on a fluorosilane coated silicon surface from Varanasi et al (μ=0.0201 N/m) was used for the predicted roll off angle calculations [19]. Tilt angle was captured discretely during the roll off method experiments with the goniometer, and the tilt angle at the time step immediately preceding the incipient motion of the drop was defined as the experimental roll off angle.

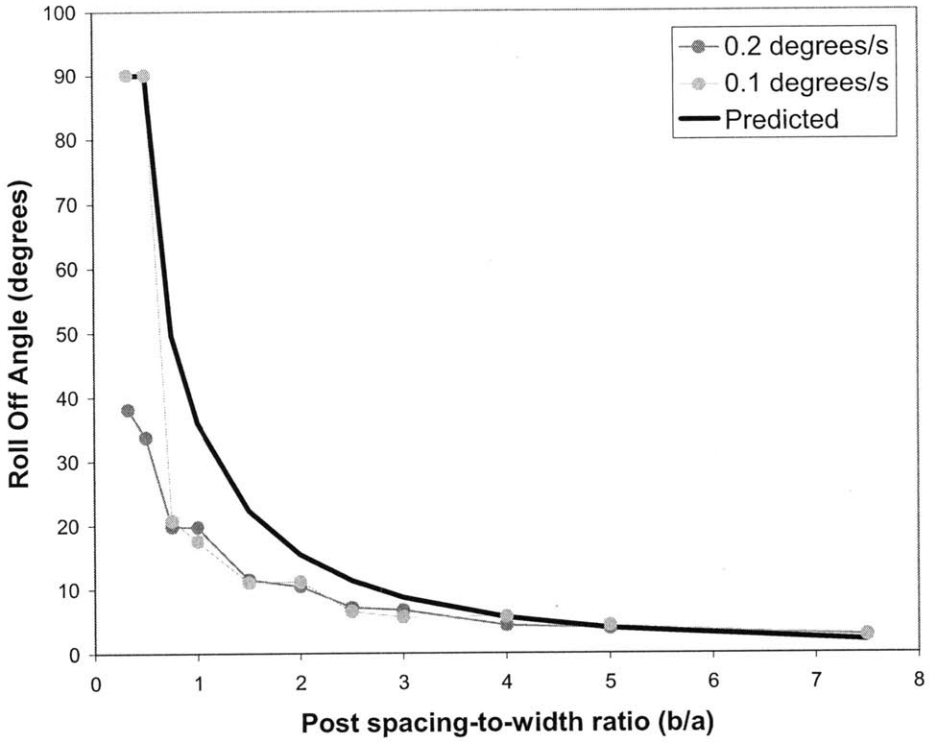

Figure 3-3: Experimentally determined and predicted roll off angles.

It should be noted that the 0.2°/s experiments were completed without the vibration damping base on the goniometer and 0.1°/s trials were completed with the vibration damping base. It was initially assumed that vibration effects resulted in the deviation of the experimental roll off angles from the predicted values; however, the addition of a vibration damping base for the 0.1°/s trials appears to have little effect on the experimental roll off angle.

Based on Figure 3-3, the overall trend of roll off angle as a function of post-spacing-to-width ratio appears to be consistent between the experimental and predicted data, and the predicted and experimental roll off angles appear to be more consistent for higher post spacing-to-width ratios. For the two tilt rates tested, it also appears that the tilt rate has a negligible effect on the resulting roll off angle.

The pinning parameter predictions of roll off angle are verified experimentally with some error. Future work with the pinning parameter will aim to define μ for dynamic cases. It is theorized that μ will vary for advancing and receding contact angle depending on the texture of the surfaces, and it is likely that μ will influence wetting in impact phenomenon, but this dependence has yet to be explored. The static and dynamic definitions of μ should be extended to include rough surfaces without geometrically defined texture features. It is more likely that a coating or spray will be applied to surfaces to improve wetting behavior in industrial applications, and the resulting coated surface cannot be neatly defined by geometric parameters but the surface profile can be determined. For industrial applications, it will be important to adapt the definition of the pinning parameter by replacing the geometric term β with a surface profile dependence that can apply to a larger variety of surfaces.

4 Motion of Contact Line and Contact Angle Hysteresis

4.1 Relationship between Contact Line and Contact Angle

The relationship between contact line motion and contact angle can help to describe the behavior of the advancing and receding contact angle for a smooth surface during volume addition and subtraction. During a volume addition and subtraction experiment, the contact angle and contact line behavior can be roughly broken into four regimes as shown in the sketch below:

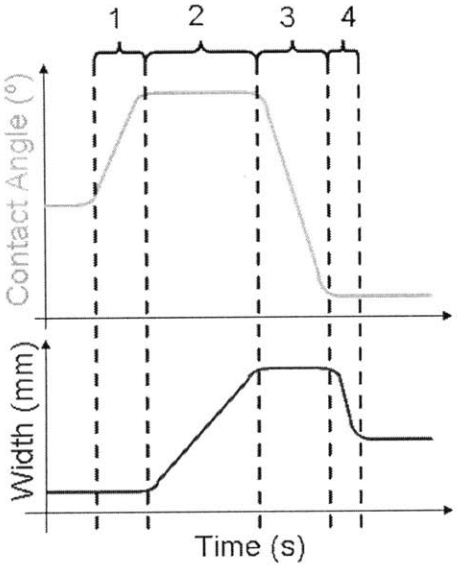

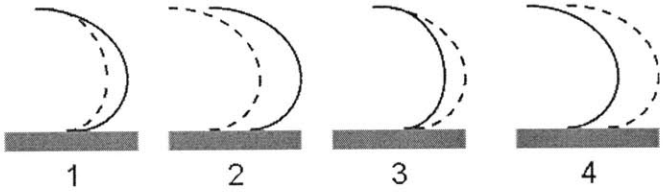

Regime	Width	Contact Angle
1	constant	increasing
2	increasing	constant at advancing angle
3	constant	decreasing
4	decreasing	constant at receding angle

Figure 4-1: Left: sketch of contact angle and width as a function of time. Top right: table of regimes with descriptions of behavior. Bottom right: sketch of drop in each regime.

On a smooth surface, a water droplet is assumed to behave according to the sketch and regimes listed above during volume addition and subtraction. The sketch is based on the contact angle, drop width, and time measured experimentally by the goniometer software. The drop width is assumed to be equal to the contact patch diameter of the droplet on the smooth surface.

Initially, a drop deposited on the substrate surface exhibits a contact angle between the advancing and receding angle. In the first regime, volume is added to the drop and the contact angle increases linearly, but the contact line remains fixed and the width of the drop remains constant. Physically, the drop is bulging about a fixed contact line and the contact angle increases as the drop bulges outward. The contact line remains pinned until the advancing contact angle is reached and the drop behavior transitions to the second regime. In the second regime, the contact line moves along the surface of the substrate maintaining a constant, advancing contact angle. The contact angle and contact line motion remain in the second regime as volume continues to be added to the drop. When volume is then subtracted, the width of the drop is initially remains constant in the third regime. Again the contact line is pinned; the drop is gradually losing volume and

physically appears to be deflating about a fixed contact line until a receding contact angle is reached. In the fourth regime, the receding angle is maintained as the width decreases linearly.

Experimentally the results should follow a similar trend with some error. The plot below shows a water drop undergoing volume addition and subtraction on a fluorosilane coated silicon wafer. The regimes corresponding to the theoretical plot are outlined.

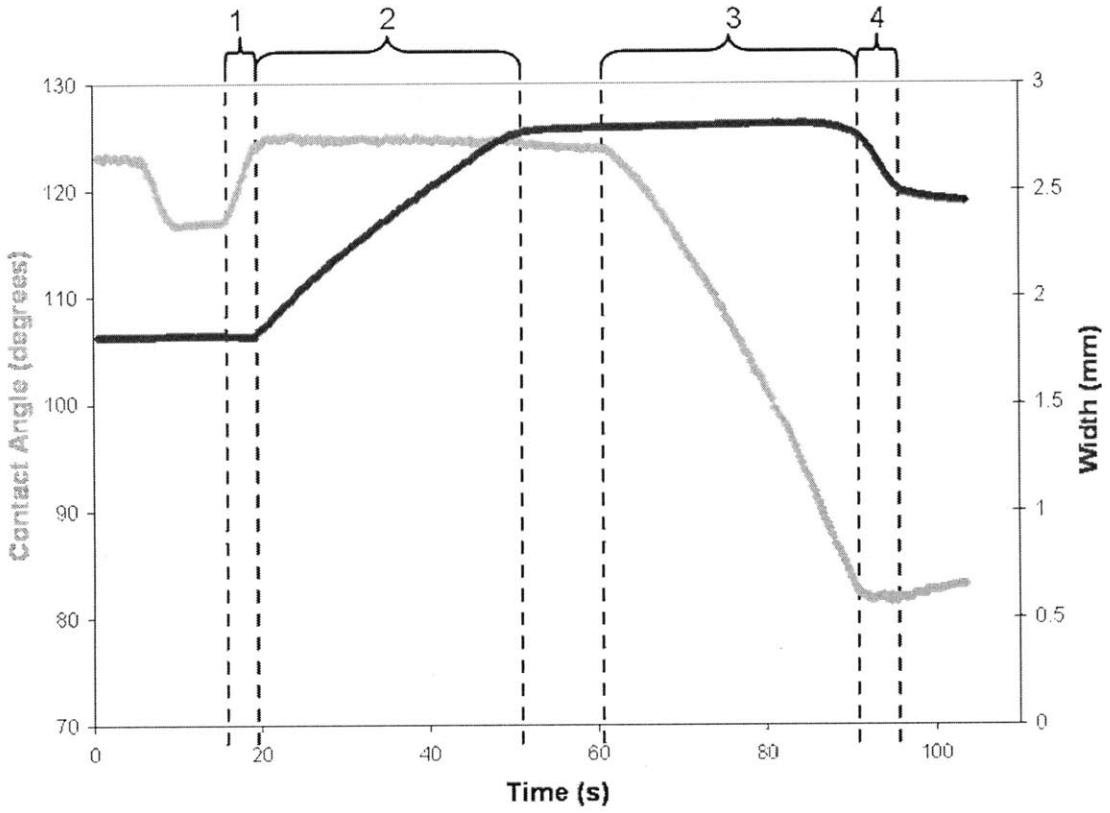

Figure 4-2: Width and contact angle vs. time for volume addition and subtraction of a water drop on a fluorosilane coated silicon substrate. Volume addition and subtraction rate set at 0.417μL/s.

It should be noted that the space between the second and third regimes is present because no liquid was added or subtracted from the drop during that time period; therefore, both the contact angle and width plots remain constant. The transitions between regimes are consistent with the theoretical plot, so the theoretical relationship described between contact line motion and contact angle for smooth surfaces should be valid experimentally.

4.2 Stick-Slip Behavior of Contact Line on Textured Surfaces – Cassie

From experimental observation, the ideal behavior of the contact angle and contact line on a smooth surface is no longer valid for drops in the Cassie state on micro-post surfaces. However, the contact line and contact angle motion can again be roughly broken into four regimes.

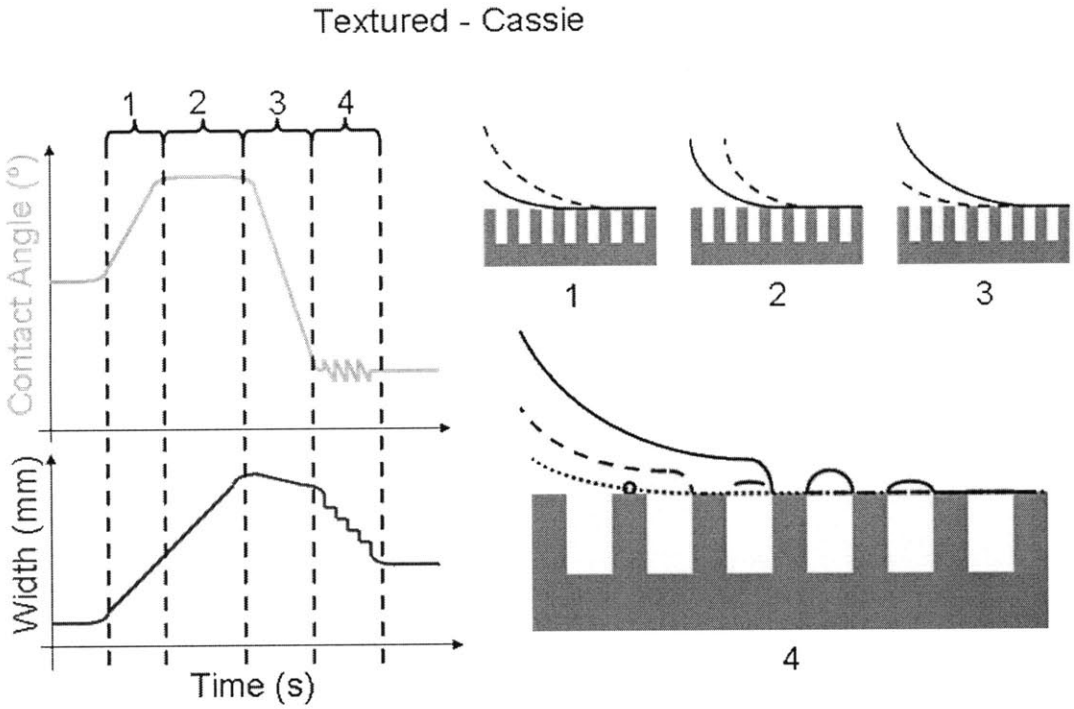

Regime	Width	Contact Angle
1	increasing	increasing
2	increasing	constant at advancing angle
3	slightly decreasing	decreasing
4	decreasing with stick-slip	at receding angle with stick-slip

Figure 4-3: Left: sketch of contact angle and width vs. time for volume addition and subtraction with Cassie drop. Right: sketch of drop contact line in each regime. Bottom: table of regimes with descriptions of behavior.

The first three regimes are relatively consistent with those observed for a smooth surface with the exception of the width behavior in the first regime. In the Cassie advancing state, it appears that the contact line advances over the micro-posts and air pockets similarly to the advancing contact line on a smooth surface. The behavior of the advancing Cassie contact line deviates from the advancing behavior on a smooth surface in the first regime when the width of the drop increases linearly as the contact angle increases. Similarly, in the initial volume subtraction in the third regime, the width of the drop appears to decrease slightly with a linear trend as the contact angle recedes, which might be related to the increase in width with advancing that occurs in the first regime.

The most extreme deviation from contact line and angle behavior from that on a smooth surface occurs with the stick-slip behavior of the contact line during receding in the fourth regime. On a smooth surface, the width of the drop continues to decrease linearly as the contact angle remains at a steady receding value. With stick-slip of the contact line, periodic deviations oscillations in contact angle occur at the receding angle. When the contact line "sticks", the width remains constant with time and the contact

angle decreases linearly. Each stick is periodically followed by a "slip" where the width rapidly decreases with nearly infinite slope and the contact angle rapidly increases similarly. Experimental plots are consistent with the theoretical plots of width and contact angle as a function of time.

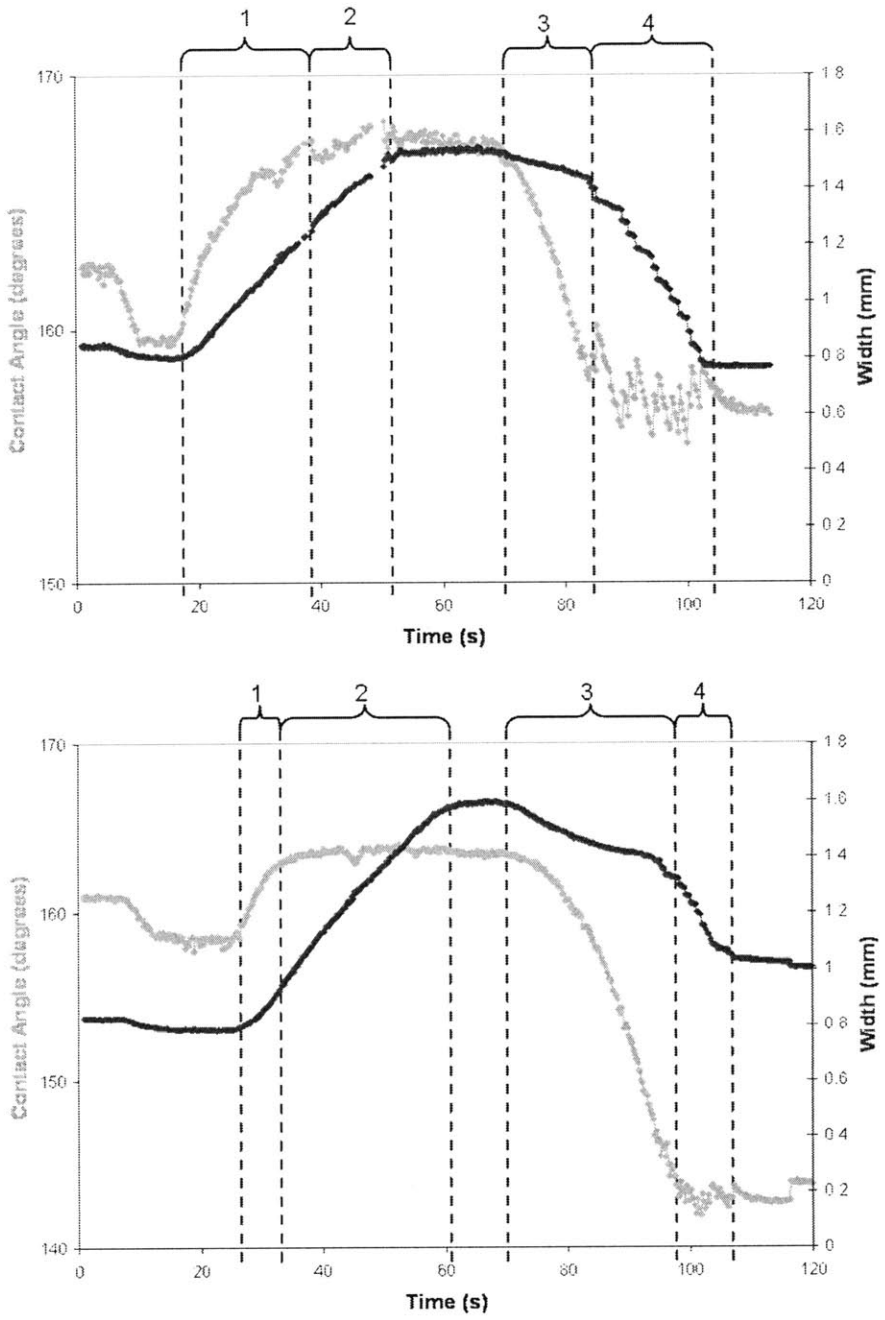

Figure 4-4: Top: contact angle and width vs. time plot for sparse post spacing (10μm by 10μm by 10μm micro-posts with 50μm spacing between posts). Bottom: angle and width vs. time plot for denser post spacing (10μm by 10μm by 10μm micro-posts with 10μm spacing between posts). Both: volume addition and subtraction rate set at 0.417μL/s.

The general trends and not magnitudes of the theoretical sketch plots are valid. The value of the advancing and receding values and the hysteresis depends on the surface and liquid. In general, surfaces with denser post spacings exhibit higher hysteresis, so the difference between the advancing and receding values is higher. It is interesting that stick-slip behavior is present in receding for both surfaces but visually, the behavior appears to occur at different amplitudes and periods.

Periodicity and amplitude of the stick-slip behavior was most visible in the sparsest post spacing. Plots of the stick-slip behavior are shown below for different sampling rates.

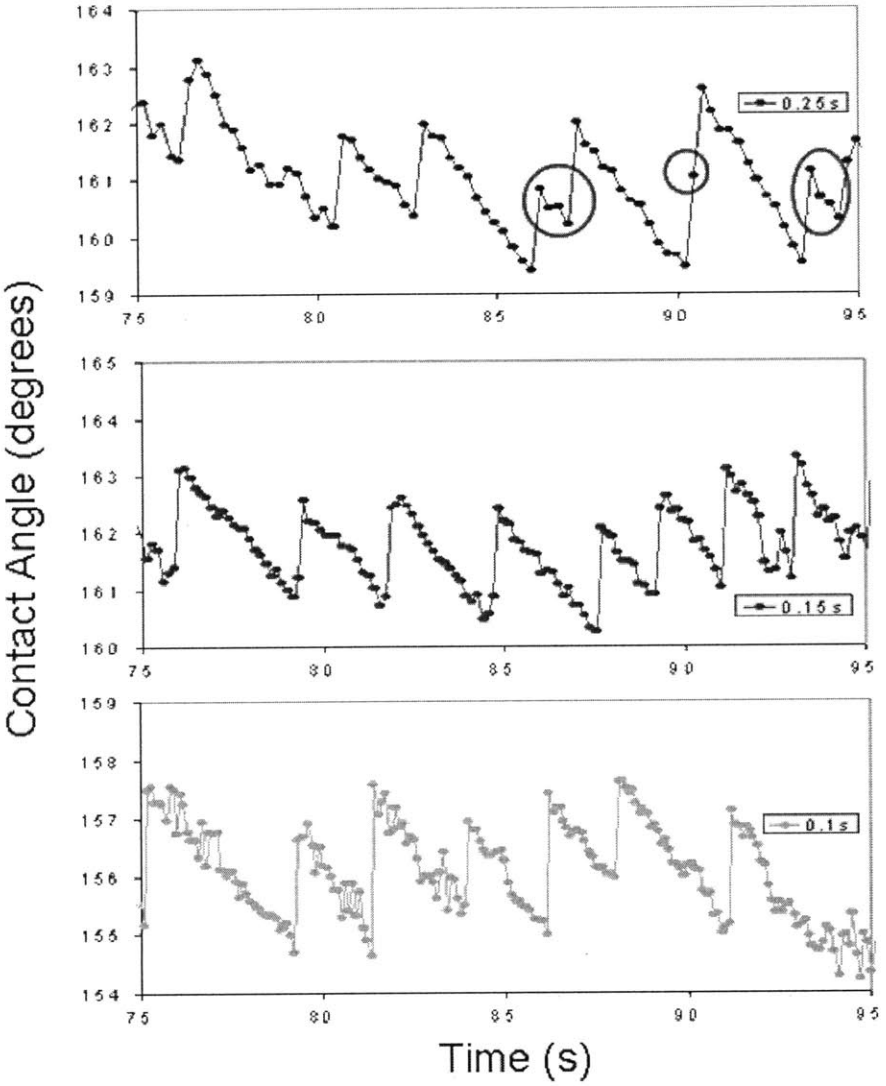

Figure 4-5: Receding stick-slip behavior in contact angle vs. time data for various time steps for samples with 75 μm spacing between posts. Measurements taken for a volume addition rate of 0.417 μL/s.

The amplitude of the stick-slip behavior was determined by averaging the peak to peak height of the saw tooth shaped contact angle vs. time curve. The period was determined

by measuring the total time of the stick slip behavior and dividing by the number of saw teeth that occurred within that time period.

It is interesting to note that the sampling rate might have an effect on the amplitude and possibly period measurements. At the highest possible sampling rate of 0.1s between measurements, there are no points between the local minima and maxima in the saw tooth function. For the lowest sampling rate of 0.25s between measurements, there are points present between a local minima and maxima, which are circled in the first plot of Figure 4-5. These additional points reflect inaccuracies in the contact angle fluctuation measurements that result from a low sampling rate. The sampling rate is too low and is therefore not capturing the peak heights and full period of each saw tooth accurately. A time step of 0.25s between measurements was commonly used for the contact angle measurements, so it is likely that there is some error in the amplitude and period values. It should be noted that sampling rate was examined for a volume addition and subtraction rate of 0.417 μL/s and changing the volume addition and subtraction rate could change the appropriate sampling parameters.

The amplitude of stick-slip behavior was plotted for different post densities and volume addition and subtraction rates.

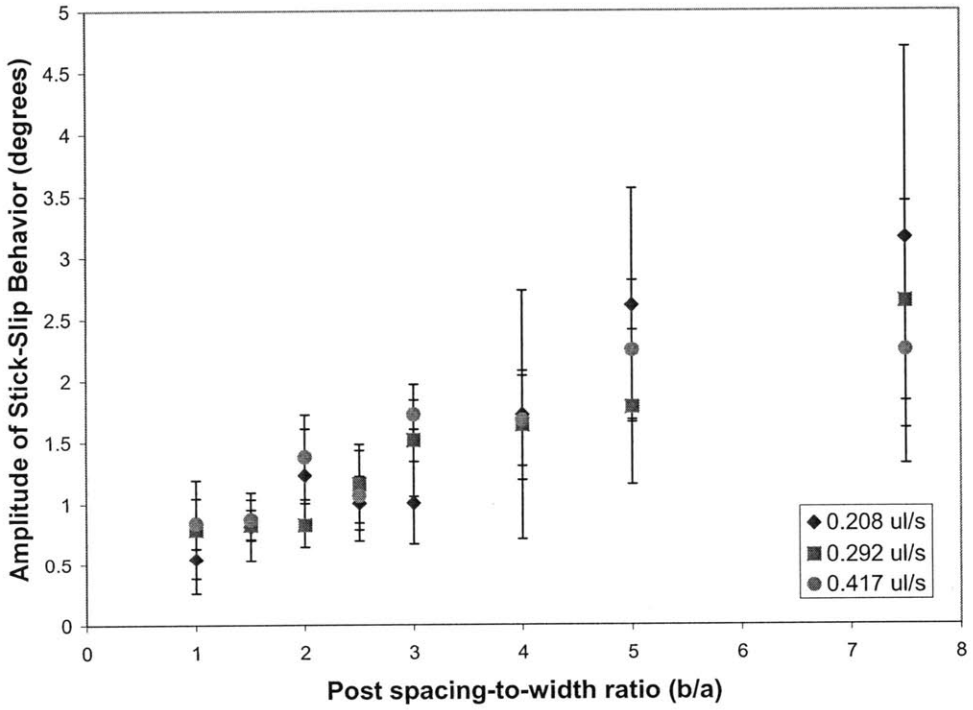

Figure 4-6: Amplitude of stick-slip receding behavior vs. post density for different volume addition and subtraction rates. Error bars indicate 95% certainty range.

As post spacing becomes sparser, the amplitude of the stick-slip behavior of the contact angle increases linearly. Amplitude data points were not collected for the densest post spacings (3.3μm, 5μm, and 7.5μm) because the amplitudes were difficult to detect and measure. However, for those surfaces, fluctuations at the receding angle were present suggesting that small amplitudes of stick-slip behavior in the contact angle occurred that might lie along the linear curve.

Physically, stick-slip behavior can be attributed to the capillary failure of capillary bridges that form between the drop and micro-post when volume is withdrawn. Water is pulled upward forming a bridge that is strained normal to the surface until the bridge fails, and the capillary dewetting likely results in the formation of small sessile drops on the surface as pictured in Figure 4-3 [28]. High speed video of volume addition and subtraction of a water drop on micro-post substrates was taken to verify the physical interpretation of the contact angle and width data.

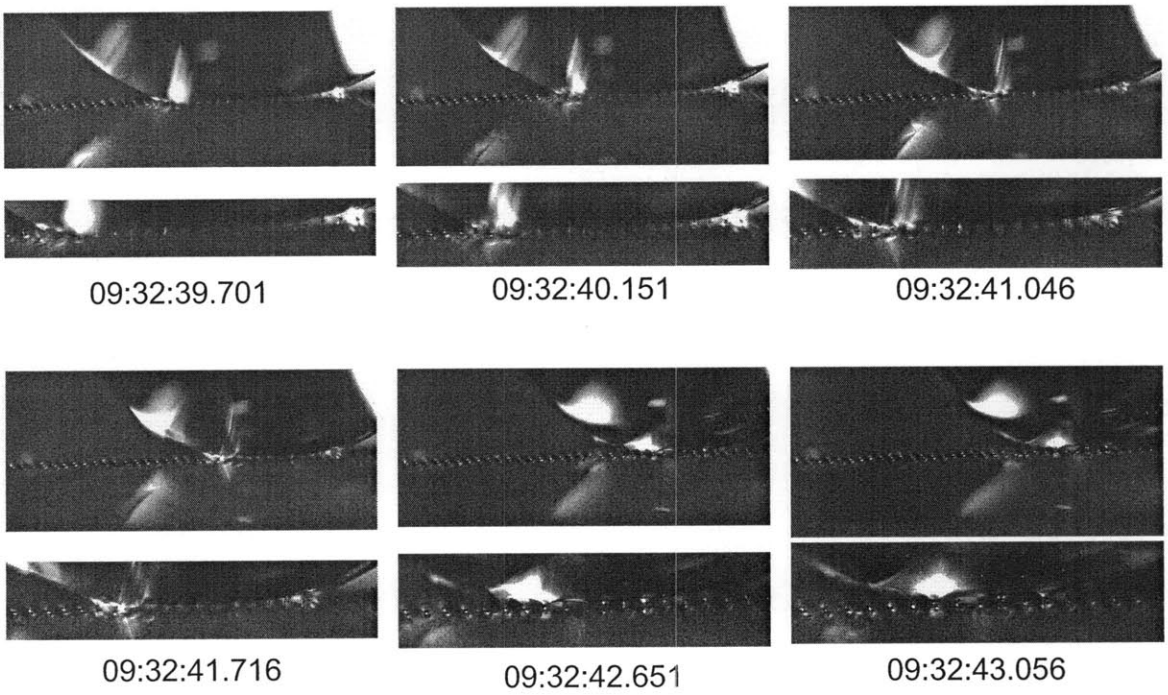

Figure 4-7: Images of high speed video of receding water drop on 10μm by 10μm by 10μm micro-posts with 50μm spacing between posts. Volume addition and subtraction rate set at 0.417 μL/s. Time of each frame is provided.

In the first video frames and at the start of volume subtraction, capillary depinning does not appear to be present and the contact angle decreases as the drop recedes, which is consistent with the predicted behavior of a Cassie drop in the third regime. As volume continues to be subtracted from the drop, capillary bridges form between the water droplet and the micro-posts pinning the drop. The capillary bridges are plucked normal to the surface as the contact line continues to recede creating the "slip" behavior in the fourth regime, and the pinning causes the contact line to periodically "stick." Both behaviors are consistent with the predicted physical behavior of the drop during receding.

High speed video of a drop was taken for an advancing drop on the same substrate with the same volume addition and subtraction rate as the video provided in Figure 4-7.

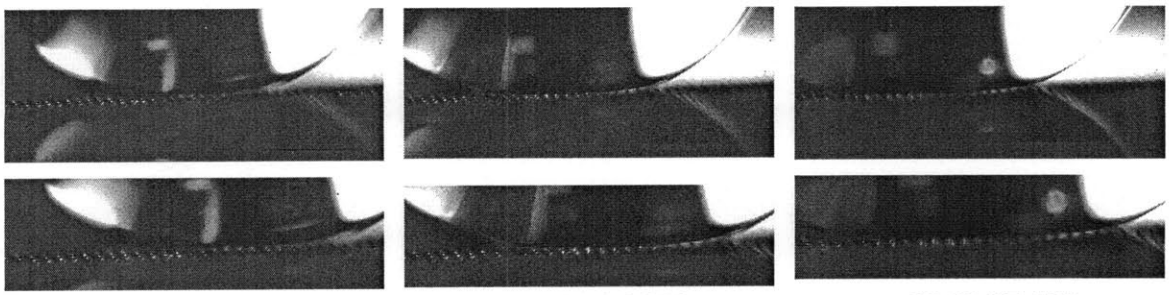

Figure 4-8: Images of high speed video of advancing water drop on 10μm by 10μm by 10μm micro-posts with 50μm spacing between posts. Volume addition and subtraction rate set at 0.417 μL/s. Time of each frame is provided.

In the final frames, the drop has expanded outside the video frame. Pinning of the drop on the micro-posts is not present along the contact line as the drop advances and the drop advances smoothly over the posts and air pockets along the substrate surface, which is consistent with theoretical predictions.

4.3 Stick-Slip Behavior of Contact Line on Textured Surfaces – Wenzel

Similar to Cassie wetting, contact line and angle behavior for droplets in the Wenzel case deviates from behavior on a smooth surface and exhibits stick-slip behavior in both advancing and receding. From experiment, the Wenzel case was examined for 10μm by 10μm by 10μm posts with 100μm post spacing, and a theoretical plot was generated based on these experiments.

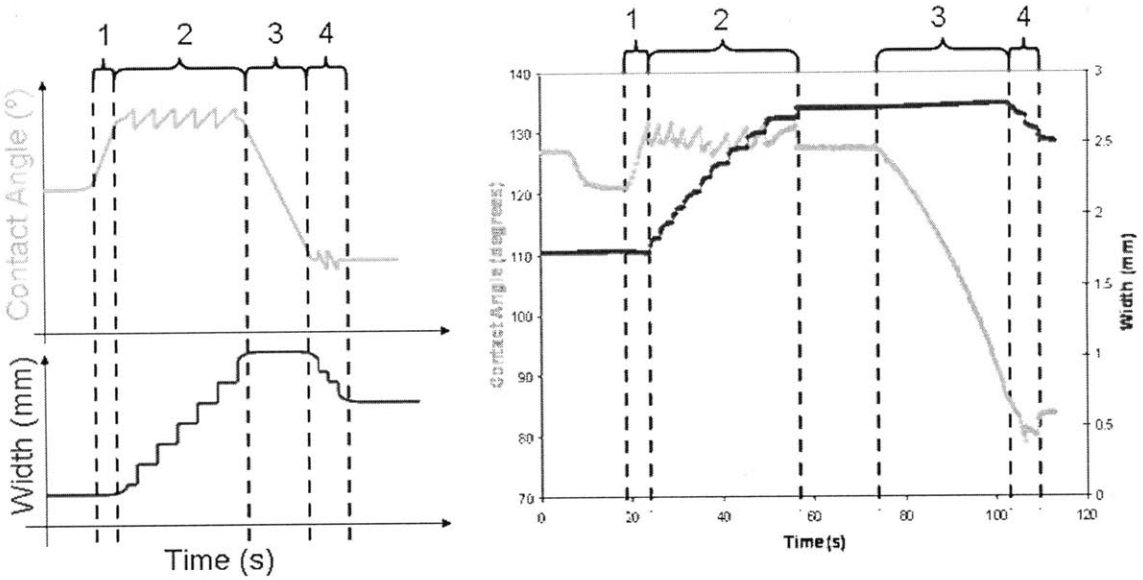

Regime	Width	Contact Angle
1	constant	increasing
2	increasing with stick-slip	at advancing angle with stick-slip
3	constant	decreasing
4	decreasing with stick-slip	at receding angle with stick-slip

Figure 4-9: Left: Contact angle and width vs. time plot for Wenzel water drop on micro-post substrate. Right: contact angle and width vs. time plot for 10μm by 10μm by 10μm micro-posts with 100μm spacing between posts. Volume addition and subtraction rate set at 0.417μL/s. Bottom: table of regimes with descriptions of behavior.

Stick-slip behavior in the receding case appears to be similar to the receding behavior in Cassie, so it is likely that capillary dewetting occurs similarly in receding for the Wenzel state. Further experiment and observation with high speed video is necessary to physically understand the receding and especially advancing behavior of Wenzel droplets.

5 Preliminary Investigation of Velocity Effects on Contact Line Motion

5.1 Volume Addition and Subtraction Rate Variation and Experimental Results

Preliminary experiments were completed to explore the effect of contact line velocity on contact angle and the motion of the contact line. Contact angle measurements using the volume addition and subtraction technique were completed at volume addition and subtraction rates of 0.208, 0.292, 0.417, 2.5 and 12.5 μL/s. A minimum of four and maximum of six trials were completed for each volume addition and subtraction rate and post spacing; the results were averaged to determine advancing and receding contact angles.

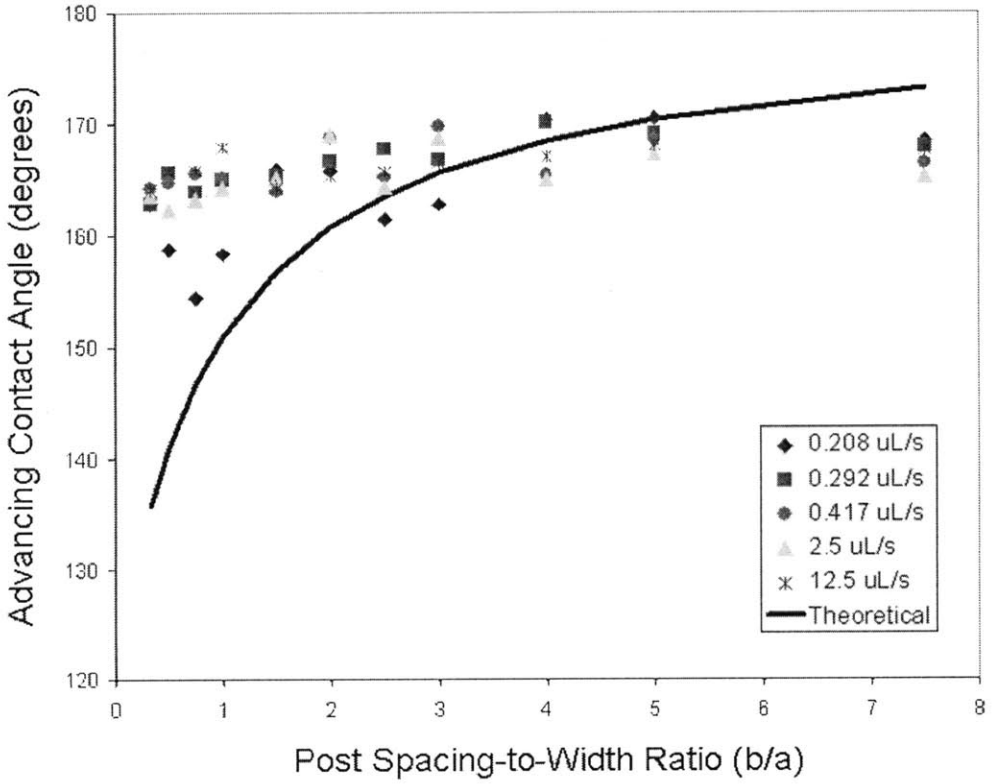

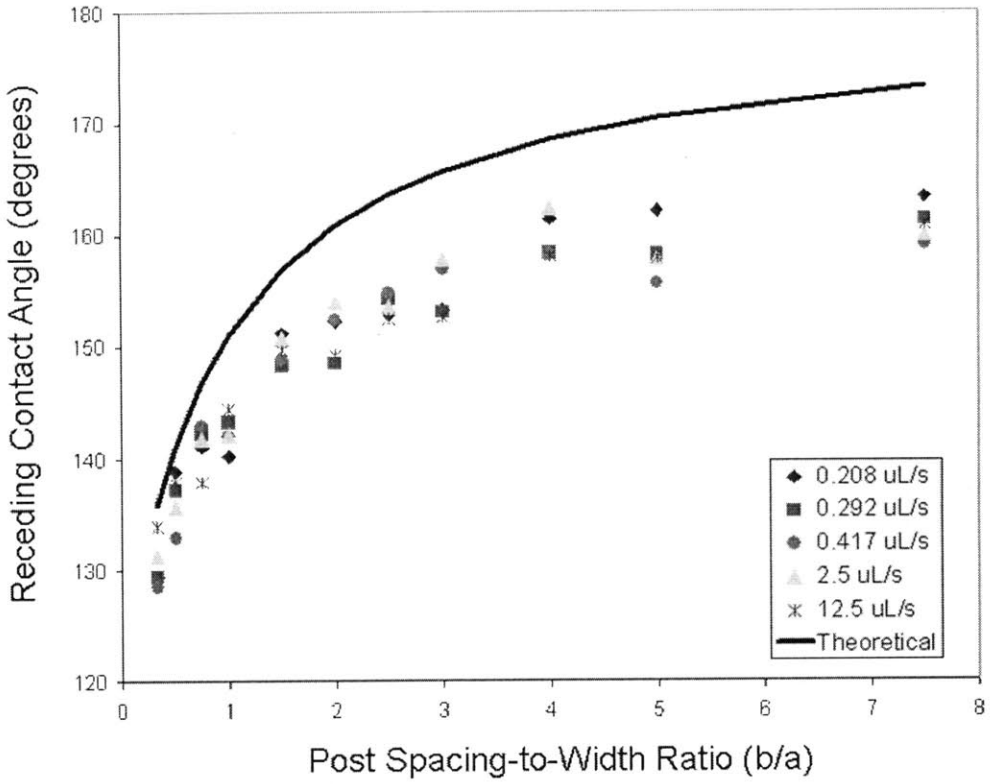

Figure 5-1: Advancing (top) and receding (bottom) contact angles measured with volume addition and subtraction method plotted against post spacing-to-width ratio.

The theoretical plot was generated from the equation for the Cassie equilibrium contact angle in equation 3-5.

The rate of volume addition and subtraction does not appear to have a quantifiable effect on the measured receding and advancing contact angles. Advancing contact angle appears to remain relatively constant with the post spacing-to-width ratio yet the receding angle follows the trend of the projected equilibrium curve. The equilibrium contact angle for the experimental data was calculated based on the advancing and receding contact angles using the Tadmor equation below [29]:

$$\theta_0 = \arccos\left(\frac{\Gamma_A \cdot \cos\theta_A + \Gamma_R \cdot \cos\theta_R}{\Gamma_A + \Gamma_R}\right) \tag{5-1}$$

where

$$\Gamma_R = \left(\frac{\sin^3\theta_R}{2 - 3\cdot\cos\theta_R + \cos^3\theta_R}\right) \tag{5-2}$$

and

$$\Gamma_A = \left(\frac{\sin^3 \theta_A}{2 - 3 \cdot \cos \theta_A + \cos^3 \theta_A} \right) \tag{5-3}$$

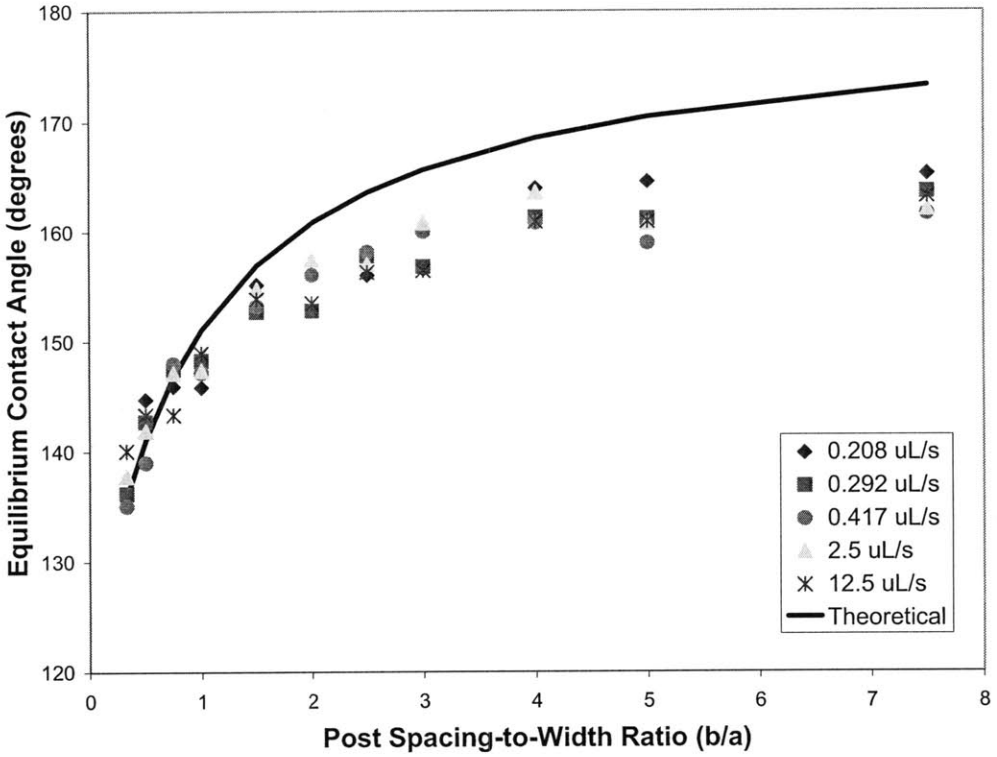

Figure 5-2: Equilibrium contact angle calculated from advancing and receding angle experimental data plotted against post spacing-to-width ratio.

The experimental equilibrium contact angle values agree with the predicted equilibrium contact angle for dense post spacings but vary from the theoretical curve as the post spacing-to-width ratio increases. This deviation pattern is consistent with the experimental values measured by Varanasi et al. From the initial experiments, it appears that the volume addition rate and therefore the contact line velocity has a negligible effect on the measured advancing and receding contact angles, but further investigation is necessary verify this assumption.

In the volume addition and subtraction experiments, it was hypothesized that increasing the volume addition and subtraction rate increased the velocity of the contact line. Experimental data was examined to test this assumption and to determine more conclusively the relationship between the volume addition and subtraction rate and contact line velocity. Contact line velocity was also examined for each surface in the advancing and receding cases to further explore the relationship between advancing and receding contact line motion and velocity. Advancing and receding contact line velocities were determined experimentally from values of drop width and measurement number captured by the goniometer software.

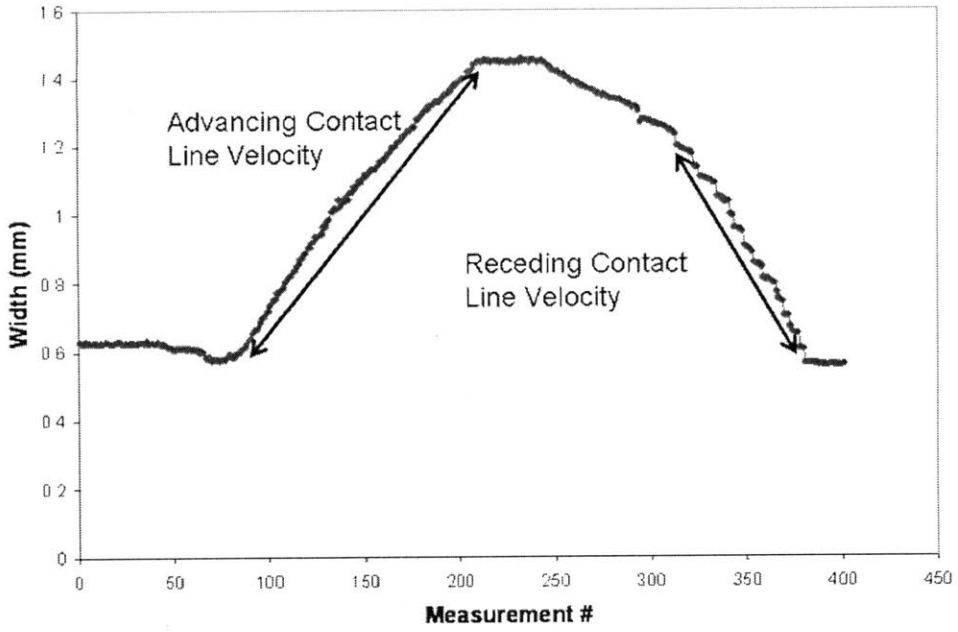

Figure 5-3: Sample plot of width against measurement number for 40 μm post spacing at 0.417 μL/s volume addition and subtraction rate.

A linear fit of the experimental values between the initial minimum and maximum width was used to determine the advancing contact line velocity value. In receding, initial decrease at a small slope was observed before steeper decay with stick-slip behavior as show in Figure 4-4. The slope of the region with steeper decay was used to determine the receding contact angle velocity linking the receding contact line velocity to the stick-slip behavior of the contact line. Slopes were divided by the time step between measurement numbers to determine contact line velocities.

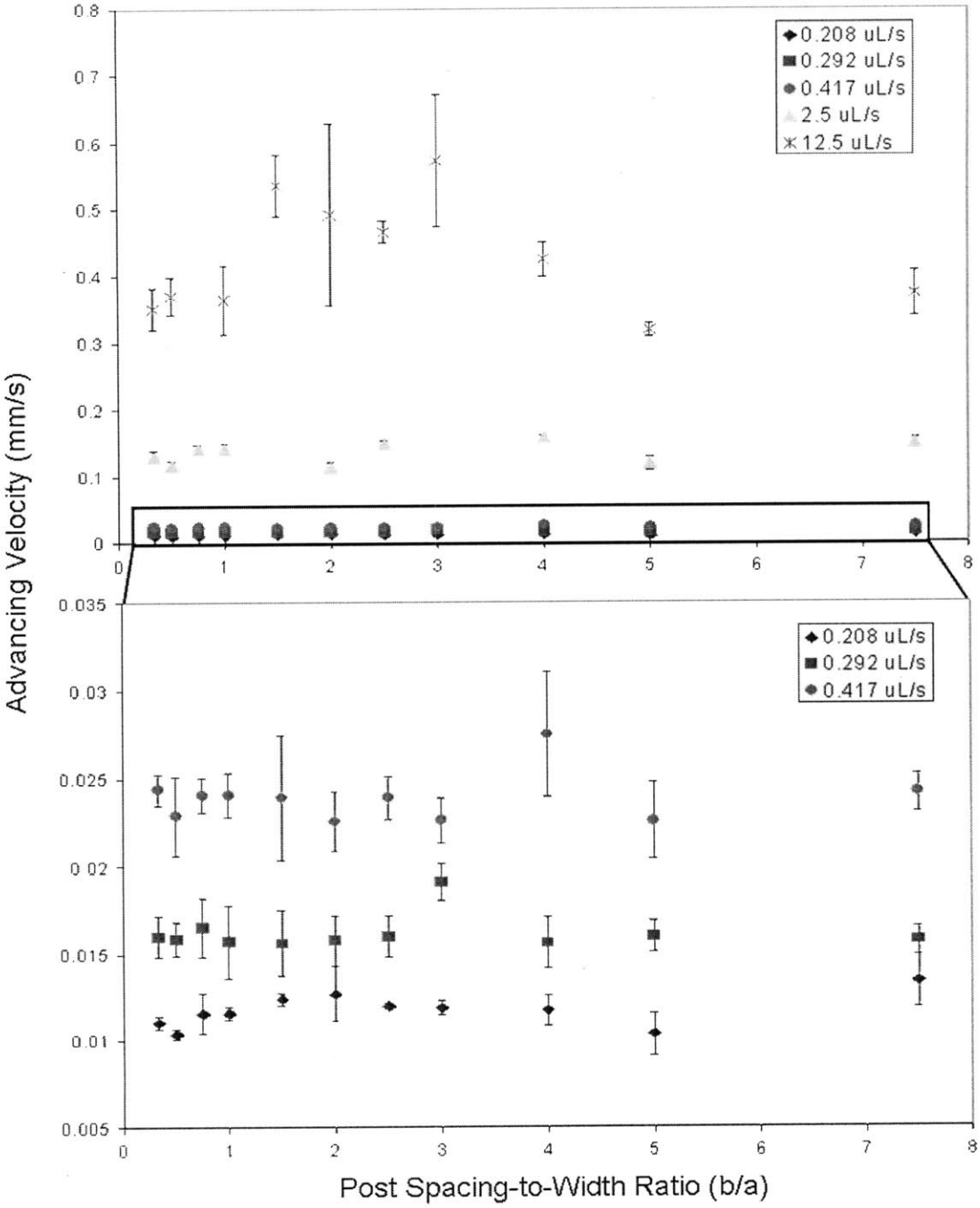

Figure 5-4: Magnitude of advancing contact line velocity plotted against post spacing-to-width ratio for various volume addition and subtraction rates. Error bars indicate 95% certainty range.

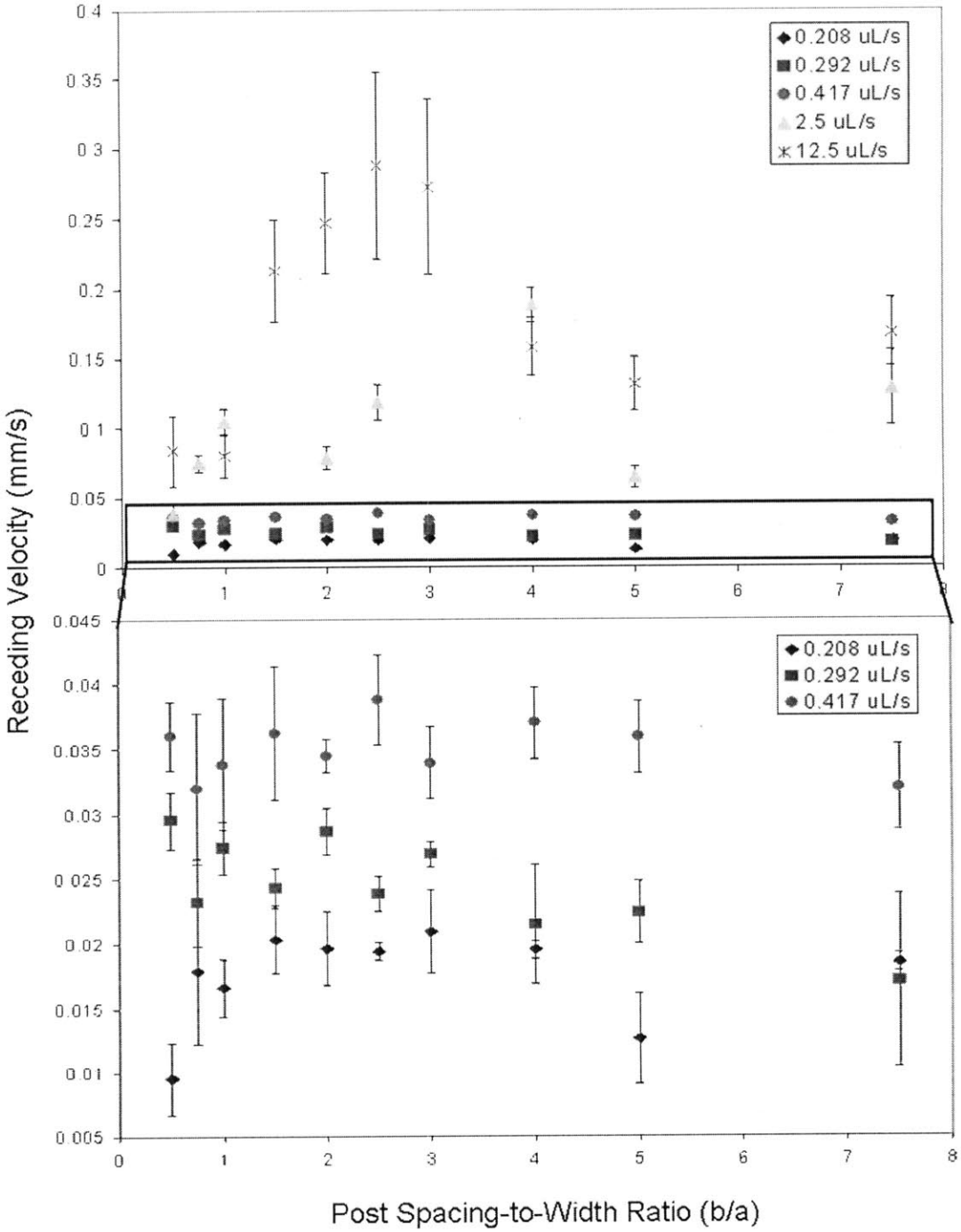

Figure 5-5: Magnitude of receding contact line velocity plotted against post spacing-to-width ratio for various volume addition and subtraction rates. Error bars indicate 95% certainty range.

As theorized, the magnitude of the advancing and receding contact line velocities increases with volume addition and subtraction rate. It appears that the contact line velocity generally remains constant with post spacing-to-width ratio, but the exact relationship is not fully discernable. Assuming the contact line velocity remains constant

with post density, a plot of the contact line velocity in the advancing and receding cases as function of the volume addition and subtraction rate was constructed to further understand the relationship between contact line velocity and volume addition rate.

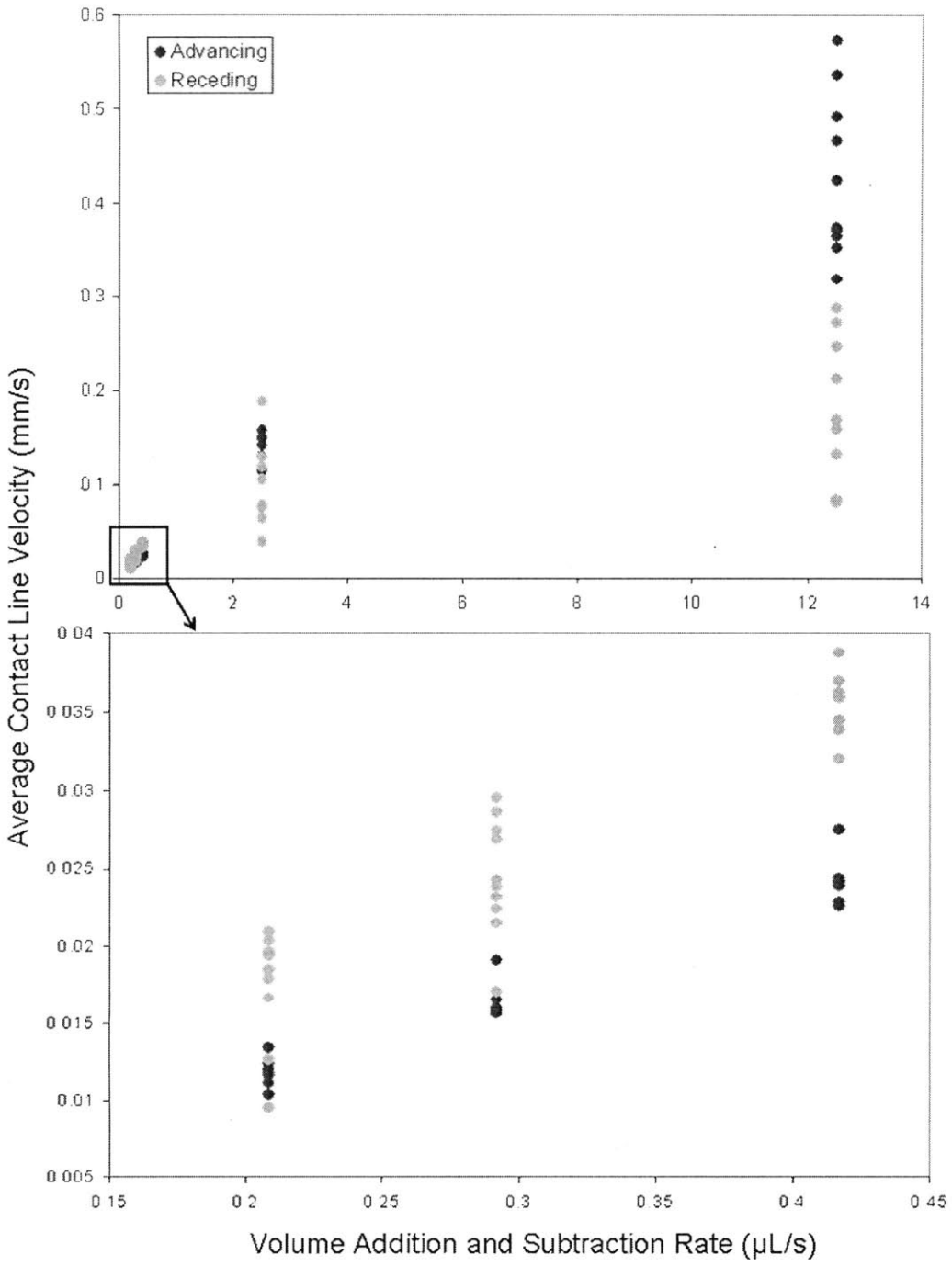

Figure 5-6: Average contact line velocity plotted against volume addition and subtraction rate. Each point is the velocity at a particular post spacing-to-width ratio.

There appears to be a roughly linear increasing relationship between the contact line velocity and the volume addition and subtraction rate, but this relationship is not fully determined. The hypothesis that contact line velocity increases with increasing

volume addition rate is confirmed. As the volume addition and subtraction rate increases, variation in contact line velocity appears to increase. It is interesting that the magnitude of the advancing and receding contact line velocity are noticeably different in the advancing and receding cases. For slower volume addition and subtraction rates including 0.208, 0.292, and 0.417 μL/s, the advancing contact line velocity is generally smaller in magnitude than in the receding case, but for higher volume addition and subtraction rates including 2.5 and 12.5 μL/s, the relationship is flipped and the advancing contact line velocities exhibit higher magnitudes. The exact relationship between advancing and receding contact line velocity and volume addition and subtraction rate should be further explored and quantified.

The noticeable difference in magnitude between the advancing and receding contact line velocity suggests that different mechanisms dictate the motion of the contact line in the advancing and receding phases supporting the physical descriptions of advancing and receding contact line described in Section 4.2. Contact line motion in the advancing case occurs with the sliding of the contact line of the water droplet over the micro-posts and air pockets, and in the receding case, the contact line is pinned at the micro-posts. The motion of the receding contact line exhibits stick-slip as a result of the pinning and contact line motion occurs with failure of the capillary bridge formed between the water droplet and micro-post resulting in depinning normal to the post surface. Since the advancing and receding contact line motion are governed by different phenomena, the advancing and receding contact line velocities will vary as a reflection of the physical interpretation of contact line motion.

5.2 Velocity Dependence of Stick-Slip Behavior

Since the contact line velocity varies with volume addition and subtraction rate, the contact line motion is affected by the contact line velocity and it seems logical that the contact line velocity should also influence the contact line motion during stick-slip behavior of the contact line. As shown in Figure 4-6, the volume addition and subtraction rate does not seem to have a discernable influence on the amplitude of the stick-slip behavior, and therefore it can be assumed that the contact line velocity also has a negligible effect on the stick-slip amplitude. The period of the stick-slip behavior was plotted as a function of the post spacing-to-width ratio and suggests that volume addition and subtraction rate affects the periodicity of stick-slip.

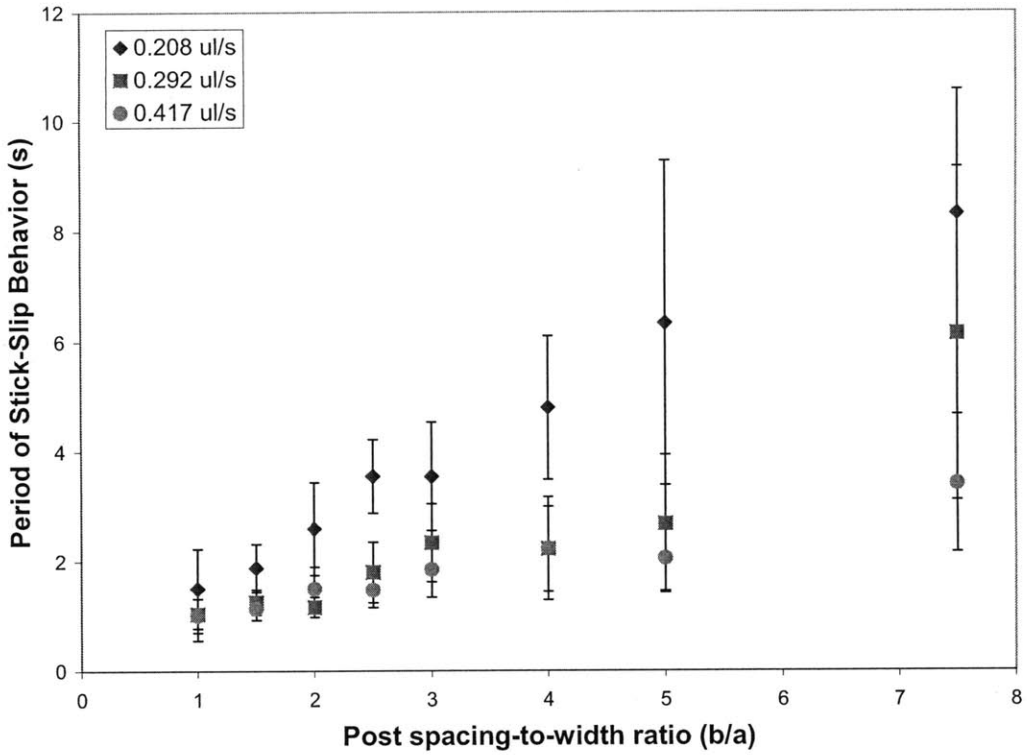

Figure 5-7: Period of stick-slip behavior as a function of post spacing-to-width ratio for various volume addition and subtraction rates. Error bars indication 95% certainty range.

As the volume subtraction rate decreases, the period of the stick-slip behavior increases and in many cases, the period doubles between the fastest and slowest volume addition rates where the slowest volume addition and subtraction rate is roughly half the speed of the fastest case. Since the period of stick-slip increases as volume subtraction rate decreases, it can be assumed that the period of stick-slip increases as the receding contact line velocity decreases.

Further detailing of the physical mechanism of receding with examination of capillary bridge force can help to theoretically interpret the relationship between stick-slip behavior and contact line velocity. For a Cassie drop during receding, the drop is pinned at posts along the contact line and with continued volume subtraction, a capillary bridge forms and grows until it ruptures creating small sessile drops on the post surface.

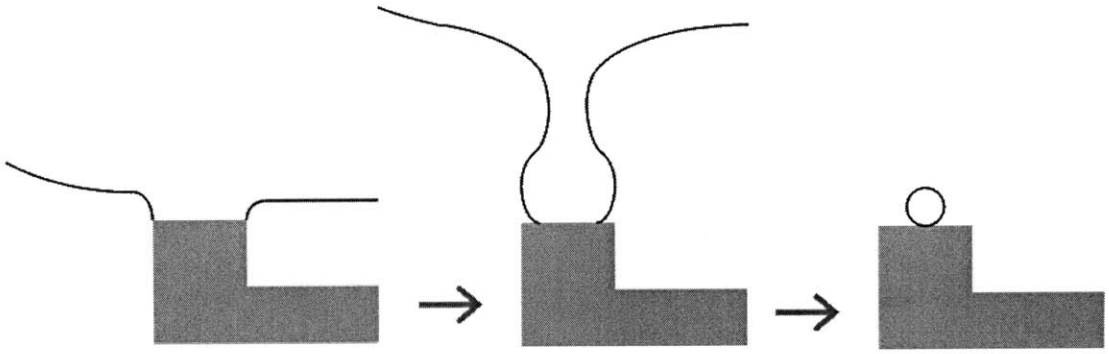

Figure 5-8: Formation and rupture of capillary bridge on micro-post during receding phase with Cassie droplet.

The receding contact angle immediately before rupture can be approximated with the equation for capillary force (F_c) given below:

$$F_c = \pi \cdot \left(r_c^2 \cdot P_c - 2 \cdot r_c \cdot \gamma_l \cdot \sin \varphi_c \right) \tag{5-4}$$

where r_c is the radius of the contact line above the neck, P_c is the capillary pressure defined as the change in pressure between the inside and outside of the drop and φ_c is the meniscus slope angle at the contact line [30].

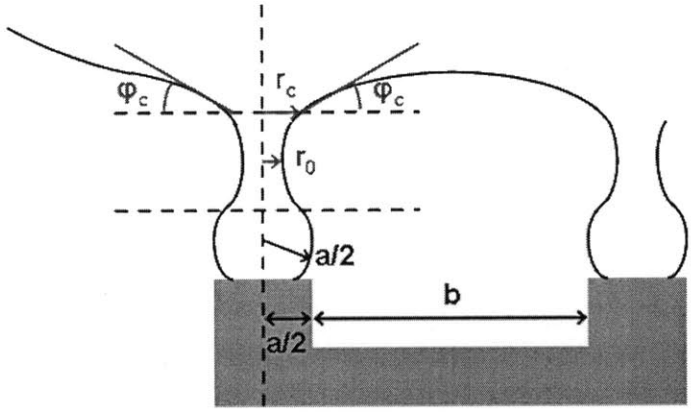

Figure 5-9: Capillary bridge on micro-post surface immediately before rupture.

Geometrically, the radius of the contact line can be approximated as the "radius" of the micro-post (a/2). The equation for capillary force is derived for the capillary bridge that forms between two axisymmetric bodies, so it is assumed that the capillary bridge forms between the small sessile drop forming in contact with the micro-post acting as one axisymmetric body and the full spherical drop acting as the another axisymmetric body. If capillary force is positive, the two bodies are repelling each other and if it is negative, the bodies are attracted. In the Cassie receding case, the drop is pinned on the micro-post surface preventing contact line motion, so the force is considered attractive and the capillary force should be negative. As the bridge ruptures, there should be no attraction or repulsion between the micro-posts and droplet, so capillary force should approach zero.

Capillary pressure varies depending on the shape of the bridge. A non-dimensionalized form of the capillary pressure is written as:

$$p = \frac{P_c \cdot r_0}{2 \cdot \gamma_l} \tag{5-5}$$

where r_0 is the neck radius pictured in Figure 5-9. Since a neck is present in the capillary bridge, p should be negative or less than 1/2. Based on the predicted geometry, the capillary bridge shape is best approximated by an unduloid, which has non-dimensional

pressure between 0 and 1/2 [30]. The shape of the bridge becomes cylindrical as p approaches 1/2, which will be used as the limiting case for the approximation of capillary pressure. Assuming p=1/2 and Fc approaches zero immediately before rupture, the meniscus slope angle of the contact line can be approximated as a function of neck radius using equation 5-5 and 5-6:

$$\varphi_c(r_0) = \arcsin\left(\frac{a}{4 \cdot r_0}\right) \tag{5-6}$$

The left, top edge of the contact line pictured in Figure 5-9 creates the contact angle immediately before rupture between the liquid drop and the surface and therefore the receding contact angle can be estimated as:

$$\theta_r(r_0) = 180° - \varphi_c(r_0) \tag{5-7}$$

for $0<r\leq a/2$.

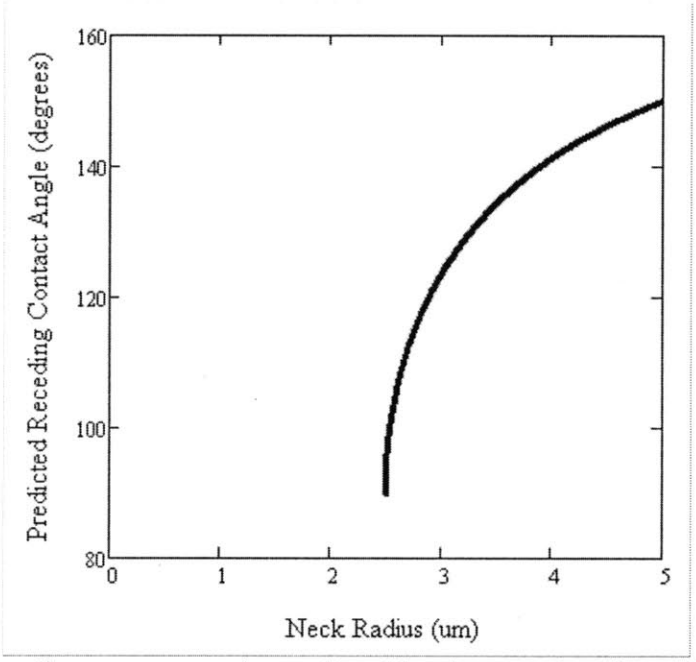

Figure 5-10: Receding contact angle predicted by the equation for capillary force as a function of neck radius.

It is interesting that the approximations of receding contact angle predicted by the capillary force model roughly fall into the range of receding contact angles experimentally determined in Figure 5-1. In this way, it seems that the neck radius must increase with post spacing, and the neck radius is likely affected by the curvature of the contact line in the spacing between posts.

From the capillary force model, assumptions about stick-slip behavior, receding contact line and velocity dependence can be tentatively drawn from these preliminary calculations. First, it can be assumed that the amplitude of the stick-slip behavior results from variations in receding contact angle between the initial capillary bridge formation

and immediately before capillary rupture. The approximation of receding contact angle generated by the capillary force model provides a minimum value of the receding contact angle and a maximum receding contact angle likely occurs when the capillary bridge is initially formed. The periodic shift between these maximum and minimum values during receding creates oscillations in the receding contact angle and generates a stick-slip amplitude. It is likely that increasing the volume addition and subtraction rate results in an increase in the period of the stick-slip behavior because the capillary bridge reaches the critical neck radius immediately preceding rupture at a faster rate. However, the geometry should not change as a function of the volume addition and subtraction rate, so the contact angle amplitude in the stick-slip behavior should not change with volume addition and subtraction rate.

6 Conclusions and Recommendations

This thesis provides a basic physical understanding with the support of experimental data of surface wetting phenomena that have yet to be fully understood: the stick-slip behavior of the contact line and a preliminary look at the influence of contact line velocity on contact line motion. It is hoped that in the future with this new understanding of these physical phenomena, hysteresis can be predicted and appropriate surfaces can be designed for drop shedding industrial applications. Separately, droplet roll off was predicted on micro-post surfaces with the pinning parameter μ experimentally determined from the advancing and receding contact angle on a smooth surface. The roll off predictions generated with the pinning parameter roughly agree with the experimentally determined roll off angles. With the pinning parameter, it is possible to predict roll off behavior for applications to the design of micro-textured surfaces. In the future, the definition of the pinning parameter should be expanded to include surface roughness, so drop roll off behavior can be predicted for a larger variety of surfaces.

In many ways, the wetting behavior of drops on superhydrophobic surfaces behaved as intuitively would be expected. With low post densities, less hysteresis is present and the contact angle increases, but upon further examination, there is complexity in the details of this behavior. As the drop advances and recedes, the behavior of the contact line changes exhibiting a saw tooth shaped periodic stick-slip behavior in contact angle. High speed video of advancing and receding behavior on micro-textured surfaces provides a broad physical understanding of the different phenomena that govern advancing and receding behavior in Cassie droplets that has been verified with experimental advancing and receding contact angle measurements. With this physical understanding, a basic model of the physical phenomena and experimental results of advancing and receding contact angle and width has been generated for the Cassie case. The stick-slip behavior of a Wenzel drop in the advancing and receding cases has been outlined and verified with experimental plots but has yet to be examined in great detail.

Future work on stick-slip behavior should aim to further quantify and detail a theoretical model of the physical behavior to allow amplitude and periodicity of the stick-slip behavior to be predicted. Contact line velocity and its influence on contact line motion and contact angle should be further examined. High speed video of the contact line at different volume addition and subtraction rates on surfaces with sparse and dense micro-post surfaces was taken to understand the motion of the contact line. Analysis of this video with tracking software could further help to quantify and provide a time scale for advancing and receding behavior for different post density surfaces. Additional high speed footage of the advancing and receding contact line for droplets in the Wenzel state could verify the model of contact angle and width behavior in the advancing and receding cases provided in Section 4.3. The focus of future work on the stick-slip behavior of hysteresis and roll off predictions of the pinning parameter should include impact phenomena, which could have exciting and broad applications in surface design for power plants and other industrial applications.

7 Appendix: Detailed Contact Angle Measurement Procedure

The document below was drawn up for the Varanasi Group as a general laboratory goniometer measurement procedure:

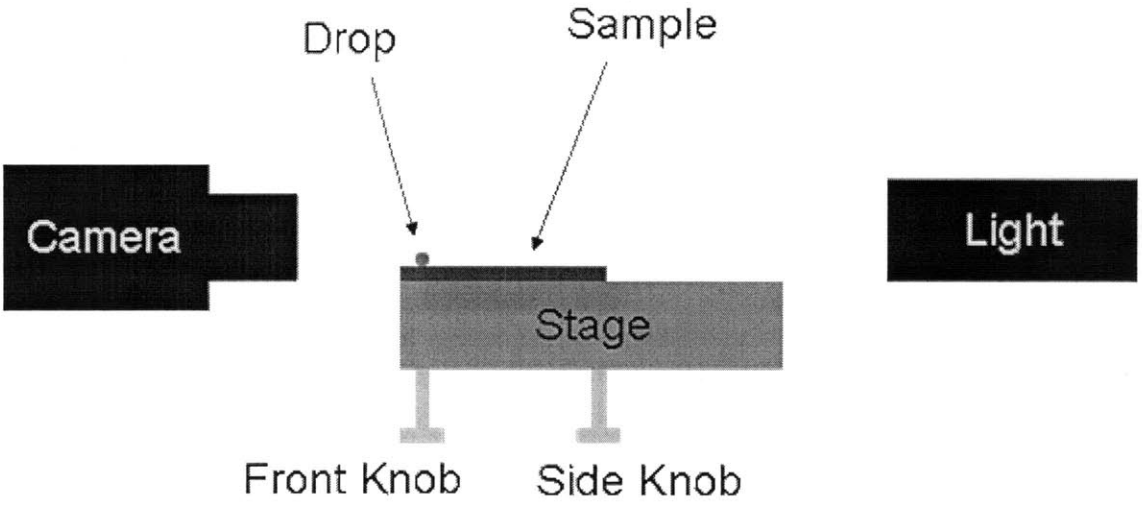

Figure 7-1: Simplified schematic of goniometer process set-up.

7.1 Sample and Drop Placement

Slide the sample to the edge of the stage closest to the camera. The front edge of the sample should lie in the same plane as the front edge of the stage. Adjust the camera so the needle is sharply focused on the screen and then a drop can be deposited. Drops should be deposited close to the front edge of the sample near the camera (refer to Figure 7-1). If the drop is not deposited close to the front of the sample, it can be difficult to insert the zero baseline because the sample surface will appear blurry.

7.2 Setting the Zero Line

Generally, zeroing can be done before and after or only after the drop has been deposited on the surface. Open the set-up interface to get a reading of the stage tilt. Before or after the drop is deposited, adjust the side knob so that the tilt reading is at or around 0.0. Once the drop is deposited, determine if the drop shadow is visible. If the shadow is not visible, adjust the front knob until the shadow becomes visible. With the shadow visible, adjust the front knob until the shadow is barely no longer visible. Turn up or down the light to get a clear baseline and drop edge, and look at the tilt reading. If the tilt reading is at 0.0, snap the zero baseline into place. If not, adjust the side knob until the tilt reading is 0.0 and snap the zero baseline.

Sometimes the baseline placement will have some visible error. For example, the droplet might lie slightly below or above the placement of the baseline. In this case, it is acceptable to adjust the baseline by hand. It appears the measurements made with a slightly low baseline tend to be more accurate than those taken with a slightly high

baseline, so if the baseline needs to be adjusted, it is better to position the zero baseline slightly too low instead of too high.

7.3 Process

Re-zero the baseline between each measurement. On each substrate, take at least four and up to six measurements. Generally, four measurements are acceptable, five or six can be taken if the results do not appear to be consistent.

It is easier to move the stage back and forth in front of the camera than to readjust the syringe between measurements. By moving the stage, it is likely that with additional measurements few adjustments will be required to zero the baseline and focus the camera on the drop. However, it is preferable to move the syringe for some measurements. Fixed syringe placement results in more precise measurements but not necessarily more accurate ones. It appears moving the syringe, refocusing and readjusting the stage will change contact line measurements slightly.

The syringe should be repositioned at least once during the four to six measurements with roughly half (usually the first 2-3 measurements) taken with the same syringe position before switching. Measurements should be taken in a grid-like pattern on the surface. Note that the syringe position should not be changed too extremely; otherwise, problems can result from depositing the droplet too far from the front edge of the stage.

7.4 Volume Addition and Subtraction Method Measurement Technique

Criteria for use: Hydrophobic and superhydrophobic substrates with advancing contact angles >120-130 degrees and hysteresis <30 degrees.

Set-Up: Use the volume addition method and parameter files saved onto the machine. The method file should be set up to take measurements every 0.25 or 0.5s, which is ideal. Verify this time step when retrieving the method file.

Note on zeroing the baseline: With the micro-post surfaces, it can be beneficial to turn the light up high so it is easier to see the micro-posts and the light that shines through those posts. When zeroing the baseline, make sure that the shadow is no longer visible, but depending on the post spacing, the posts might still be visible. Turn the light down (posts will likely no longer be visible) and then snap the baseline in place for measurements with the directions given in the general procedure.

Steps:

1. Deposit 6ul at 500s stroke time.
2. Set the zero baseline (with directions provided in general procedure).
3. Initiate measurement.
    a. Place cursors on either side of the bright spot in the center of the drop. If possible, provide some extra space between the bright spot and cursor

placement because the bright spot can expand and negatively affect contact line measurement during volume addition.

b. Click measure.

4. Withdraw 1ul at 1200s stroke time.
5. Wait until droplet appears to reach a stable volume.
6. Add 14ul at 1200s stroke time.
7. Wait until droplet appears to reach a stable volume.
8. Withdraw 14ul at 1200s stroke time.
9. Wait until droplet appears to reach a stable volume.
10. Abort experiment.

Unless otherwise specified, perform advancing and receding measurements with 1200s stroke time. Initial droplet deposition can occur at a slightly higher rate with a 400-500s stroke time. Higher stroke times are also possible but depend on the needle because bubbles can be introduced into the line, which should be avoided.

After the experiment, plot the mean contact angle and the width as a function of measurement number to interpret the results. In general trend, the contact angle curve should look something like this:

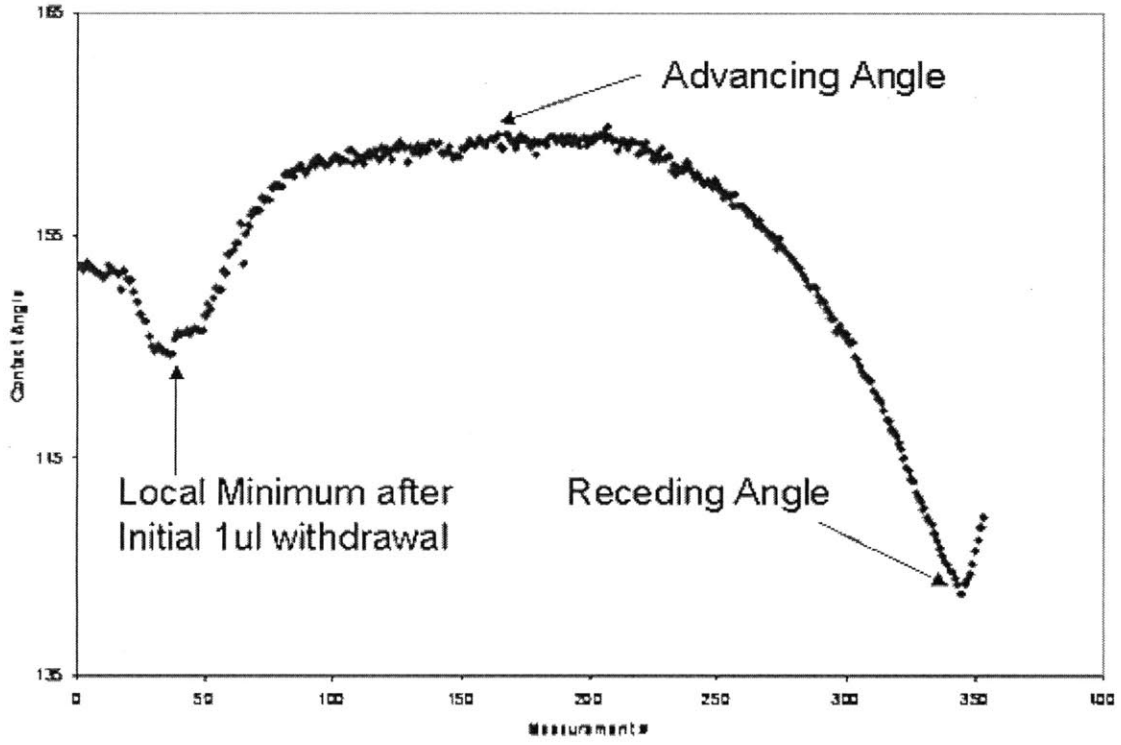

Figure 7-2: Sample contact angle vs. measurement number curve for fluorosilane coated 10μm by 10μm micro-posts with 5μm spacing between posts.

From the plot above, the average of the plateau should be considered the advancing angle and the minimum of the plot is the receding contact angle. In some cases the receding

angle reaches a steady value, so the receding angle should be calculated by taking the average of the plateau of receding values.

7.5 Roll Off Method Measurement Technique

Set-Up: Use the roll off method and parameter files saved onto the machine. In the experiment set-up, there is a section to fill in the initial and final base tilt angles for measurement. The initial and final tilt angles will vary based on the substrate and should be changed with the experimental set-up start page.

The initial and final base tilt angles should be set based on the known roll off tilt angle for the particular substrate. If the tilt angle is not known, different ranges should be tested to determine the roll off tilt angle and based on that angle, an angle range for your experiments can be determined. For a set of trials, the increment between the initial and final tilt angles should be kept constant and relatively small. Increments of 5 and 10 degrees have been used successfully in previous trials. It has been observed that the base will tilt at a rate dependent on the tilt angle range, so it is important to keep the range similar for all measurements even if the roll off angle with the substrate varies.

Steps:

1. Tape the sample down to the base.
2. Deposit 6ul at 500s stroke time.
3. Raise the syringe so it is no longer visible to the camera.
4. Set the zero baseline (with the directions provided in general procedure).
5. Open the tilting base menu and rotate the base to the starting angle specified in the experimental set-up start page.
6. Click to start the experiment. Place the right cursor relatively far to the right of the droplet without exiting the drop outline. Place the left cursor directly to the left of the light spot in the drop center.
7. Click measure. All measurements should be taken automatically. After the droplet rolls off, abort the experiment or the experiment should terminate independently.

After the experiment, plot the left and right contact angles against the measurement number. A sample trend is shown below:

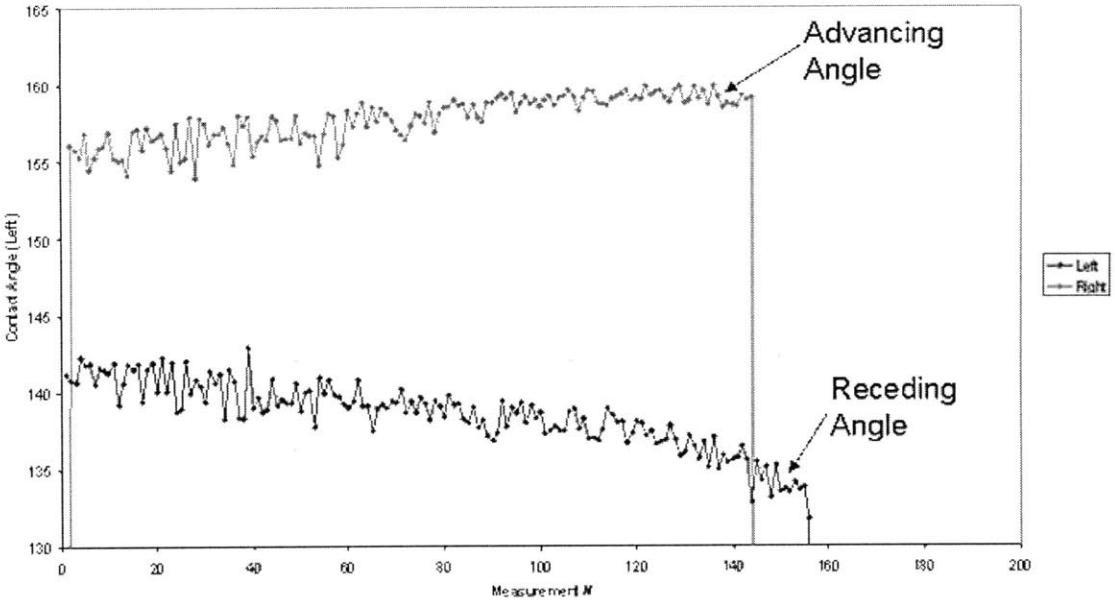

Figure 7-3: Sample right and left contact angle vs. measurement number curve for fluorosilane coated 10μm by 10μm micro-posts with 7.5μm spacing between posts.

The advancing angle is the maximum of the right angle and the receding angle is the minimum of the left angle.

8 Appendix: Derivation of Contact Patch Radius, r

Patch radius r can be written as a function of contact angle and volume from the volume of a spherical cap. A similar derivation was completed by Tadmor to determine the rate of change of the area of liquid-vapor and solid-liquid interfaces of a drop [29]. Assuming that the drop forms a spherical cap on the solid surface, the schematic below can be used as a model.

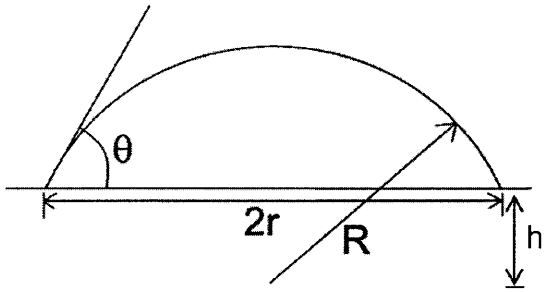

Figure 8-1: Cross-section of spherical cap with radius R on solid surface with contact patch radius r. The distance from the sphere center to the surface is h [29].

Geometrically, r and h are related to the drop radius by:

$$r = R \cdot \sin\theta \text{ and } h = R \cdot \cos\theta \tag{8-1}$$

The volume of the spherical cap is the volume of the cone beneath the surface subtracted from the total volume of the cone and spherical cap.

$$V = \left[\int_{\varphi=0}^{2\cdot\pi}\int_{\alpha=0}^{\theta}\int_{r=0}^{R} r^2 \cdot \sin\alpha \cdot d\varphi \cdot d\alpha \cdot dr\right] - \left[\frac{1}{3}\cdot\pi\cdot r^2\cdot h\right] \tag{8-2}$$

which simplifies to:

$$V = \frac{\pi \cdot R^3}{3}\cdot\left(2 - 3\cdot\cos\theta + \cos^3\theta\right) \tag{8-3}$$

and written as R in terms of V becomes:

$$R = \left[\frac{3\cdot V}{\pi\cdot\left(2 - 3\cdot\cos\theta + \cos^3\theta\right)}\right]^{\frac{1}{3}} \tag{8-4}$$

The contact patch radius equation 3-8 is simply computed by combining the equation for the spherical cap radius in 6-4 and the equation for contact patch radius in 6-1.

Bibliography

1. Hong Zhao and Daniel Beysens, "From Droplet Growth to Film Growth on a Heterogeneous Surface: Condensation Associated with a Wettability Gradient," *Langmuir* 11, no. 2 (February 1, 1995): 627-634.
2. Ashutosh Shastry, Marianne J Case, and Karl F Böhringer, "Directing droplets using microstructured surfaces," *Langmuir: The ACS Journal of Surfaces and Colloids* 22, no. 14 (July 4, 2006): 6161-6167.
3. Manoj K. Chaudhury and George M. Whitesides, "How to Make Water Run Uphill," *Science* 256, no. 5063 (June 12, 1992): 1539-1541.
4. David Quere, "Non-sticking drops," *Reports on Progress in Physics* 68, no. 11 (2005): 2495-2532.
5. Robert N. Wenzel, "Resistance of Solid Surfaces to Wetting by Water," *Industrial & Engineering Chemistry* 28, no. 8 (1936): 988-994.
6. A. B. D. Cassie and S. Baxter, "Wettability of porous surfaces," *Transactions of the Faraday Society* 40 (1944): 546-551.
7. A. B. D. Cassie, "Contact angles," *Discussions of the Faraday Society* 3 (1948): 11-16.
8. Robert J. Good, "Contact angle, wetting, and adhesion: a critical review," *Journal of Adhesion Science and Technology* 6 (1992): 1269-1302.
9. Bharat Bhushan and Yong Chae Jung, "Micro- and nanoscale characterization of hydrophobic and hydrophilic leaf surfaces," *Nanotechnology* 17, no. 11 (2006): 2758-2772.
10. Martin E. R. Shanahan, "Simple Theory of "Stick-Slip" Wetting Hysteresis," *Langmuir* 11, no. 3 (March 1, 1995): 1041-1043.
11. Rulon E. Johnson and Robert H. Dettre, "Contact Angle Hysteresis. III. Study of an Idealized Heterogeneous Surface," *The Journal of Physical Chemistry* 68, no. 7 (July 1, 1964): 1744-1750.
12. Robert H. Dettre and Rulon E. Johnson, "Contact Angle Hysteresis. IV. Contact Angle Measurements on Heterogeneous Surfaces1," *The Journal of Physical Chemistry* 69, no. 5 (May 1, 1965): 1507-1515.
13. J. F. Joanny and P. G. de Gennes, "A model for contact angle hysteresis," *The Journal of Chemical Physics* 81, no. 1 (July 1, 1984): 552-562.
14. P. Collet et al., "Dynamics of the Contact Line: Contact Angle Hysteresis," *Physical Review Letters* 79, no. 19 (November 10, 1997): 3704.
15. Y. L. Chen, C. A. Helm, and J. N. Israelachvili, "Molecular mechanisms associated with adhesion and contact angle hysteresis of monolayer surfaces," *The Journal of Physical Chemistry* 95, no. 26 (December 1, 1991): 10736-10747.
16. Jian Z. Chen et al., "Effect of contact angle hysteresis on thermocapillary droplet actuation," *Journal of Applied Physics* 97, no. 1 (January 1, 2005): 014906-9.
17. C.W. Extrand and Y. Kumagai, "An Experimental Study of Contact Angle Hysteresis," *Journal of Colloid and Interface Science* 191, no. 2 (July 15, 1997): 378-383.
18. X. F. Yang, "Equilibrium contact angle and intrinsic wetting hysteresis," *Applied Physics Letters* 67, no. 15 (October 9, 1995): 2249-2251.

19. Kripa K. Varanasi et al., "Design of Superhydrophobic Surfaces for Optimum Roll-Off and Droplet Impact Resistance," *ASME International Mechanical Engineering Congress and Exposition* (October 31-November 6, 2008): IMECE2008-67808.
20. C. W. Extrand, "A Thermodynamic Model for Contact Angle Hysteresis," *Journal of Colloid and Interface Science* 207, no. 1 (November 1, 1998): 11-19.
21. A.I. ElSherbini and A.M. Jacobi, "Retention forces and contact angles for critical liquid drops on non-horizontal surfaces," *Journal of Colloid and Interface Science* 299, no. 2 (July 15, 2006): 841-849.
22. Ilker S. Bayer and Constantine M. Megaridis, "Contact Angle Dynamics in Droplets Impacting on Flat Surfaces with Different Wetting Characteristics," *Journal of Fluid Mechanics* 558, no. -1 (2006): 415-449.
23. Junfeng Zhang and Daniel Y. Kwok, "Contact Line and Contact Angle Dynamics in Superhydrophobic Channels," *Langmuir* 22, no. 11 (May 1, 2006): 4998-5004.
24. W. Barthlott and C. Neinhuis, "Purity of the sacred lotus, or escape from contamination in biological surfaces," *Planta* 202, no. 1 (April 7, 1997): 1-8.
25. Yong Chae Jung and Bharat Bhushan, "Contact angle, adhesion and friction properties of micro-and nano-patterned polymers for superhydrophobicity," *Nanotechnology* 17, no. 19 (2006): 4970-4980.
26. C. W. Extrand, "Model for Contact Angles and Hysteresis on Rough and Ultraphobic Surfaces," *Langmuir* 18, no. 21 (October 1, 2002): 7991-7999.
27. ramé-hart instrument co., www.ramehart.com.
28. Joseph W. Krumpfer and Thomas J. McCarthy, "Contact angle hysteresis: a different view and a trivial recipe for low hysteresis hydrophobic surfaces," *Faraday Discussions: The Royal Society of Chemistry* 146 (2010): 1-9.
29. Rafael Tadmor, "Line Energy and the Relation between Advancing, Receding, and Young Contact Angles," *Langmuir* 20, no. 18 (2004): 7659-7664.
30. Peter A. Kralchevsky and Kuniaki Nagayama, *Particles at Fluid Interfaces and Membranes: Attachment of Colloid Particles and Proteins to Interfaces and Formation of Two-Dimensional Arrays*, *Elsevier* (2001): 469-502.